

# A modified combined active-set Newton method for solving phase-field fracture into the monolithic limit

Leon Kolditz<sup>1</sup>, Katrin Mang<sup>2</sup>, and Thomas Wick<sup>1,3</sup>

<sup>1</sup>Leibniz Universität Hannover, Institute of Applied Mathematics, Welfengarten 1, 30167  
Hannover, Germany

<sup>2</sup>Leibniz Universität Hannover, Institute of Structural Analysis, Appelstrasse 9A, 30167  
Hannover, Germany

<sup>3</sup>Université Paris-Saclay, LMPS - Laboratoire de Mécanique Paris-Saclay, 91190  
Gif-sur-Yvette, France

## Abstract

In this work, we examine a numerical phase-field fracture framework in which the crack irreversibility constraint is treated with a primal-dual active set method and a linearization is used in the degradation function to enhance the numerical stability. The first goal is to carefully derive from a complementarity system our primal-dual active set formulation, which has been used in the literature in numerous studies, but for phase-field fracture without its detailed mathematical derivation yet. Based on the latter, we formulate a modified combined active-set Newton approach that significantly reduces the computational cost in comparison to comparable prior algorithms for quasi-monolithic settings. For many practical problems, Newton converges fast, but active set needs many iterations, for which three different efficiency improvements are suggested in this paper. Afterwards, we design an iteration on the linearization in order to iterate the problem to the monolithic limit. Our new algorithms are implemented in the programming framework pfm-cracks [T. Heister, T. Wick; pfm-cracks: A parallel-adaptive framework for phase-field fracture propagation, *Software Impacts*, Vol. 6 (2020), 100045]. In the numerical examples, we conduct performance studies and investigate efficiency enhancements. The main emphasis is on the cost complexity by keeping the accuracy of numerical solutions and goal functionals. Our algorithmic suggestions are substantiated with the help of several benchmarks in two and three spatial dimensions. Therein, predictor-corrector adaptivity and parallel performance studies are explored as well.

**Keywords:** phase-field fracture ; complementarity system ; primal-dual active set ; modified Newton's method ; monolithic scheme ; adaptive finite elements

**This manuscript has been accepted for publication in the Journal Computer Methods in Applied Mechanics and Engineering under the DOI <https://doi.org/10.1016/j.cma.2023.116170>.**

# 1 Introduction

This work is devoted to the cost-efficient numerical quasi-monolithic solution of phase-field fracture problems. Since the pioneering studies from [25, 14] and [58, 47], the variational phase-field approach to fracture has gained a lot of attention. Summaries and overview monographs include [12, 3, 81, 78, 13, 21], and recent current trends are outlined in selected chapters in [1].

Specifically, various algorithms and numerical studies on the nonlinear and linear solution have been undertaken to date. In principle, iterative coupling (operator splitting; alternating minimization; staggered; partitioned) and monolithic approaches are distinguished. In the early work, only iterative algorithms were used [14], for which convergence results could be established theoretically [11, 17], and extended to adaptive discretizations [18]. Furthermore, [57] introduced as well operator splitting together with a strain history function for crack irreversibility. Recent promising advancements in partitioned schemes include [73, 56, 52] and some of the following references do also consider partitioned approaches as we will mention.

The first monolithic solution methods date back to [27, 77, 76]. Concerning the arising linear systems within the nonlinear iterations, the first significant study on linear solvers for phase-field fracture problems was done in [24]. More recently, further monolithic approaches were implemented in [44, 45, 49, 48, 75, 46] and a truncated non-smooth Newton multigrid solver was proposed in [31]. In [55, 69, 10] an arc-length approach was introduced in order to enhance the robustness of the solution process. Specifically, in [69, 75] comparisons of monolithic and partitioned methods were undertaken. Moreover, in Abaqus [62], implementations with comparisons between monolithic and partitioned schemes have been considered over the last years [63, 50]. As investigated in [80], classical Newton methods fail to converge for large incremental steps. Thus, monolithic solution approaches often extend and modify the Newton method to improve its stability. In order to increase the robustness, quasi-monolithic approaches were first proposed in [32] in which in one single term, actually in the quasi-linear displacement equation, an explicit linearization of the phase-field variable is introduced, but otherwise the system is still solved in a monolithic fashion. This linearization is performed in two different ways: As a first approach, the solution of the previous incremental step replaces the unknown phase-field in the displacement equation. In a second approach, to enhance the accuracy, an extrapolation of two previous incremental steps is used as an approximation. This system is numerically very robust and a block-diagonal preconditioner with algebraic multigrid preconditioning yields an efficient parallel solution [33] with an open-access implementation in [34]. This quasi-monolithic approach was also used in [40] in which a geometric matrix-free multigrid method was employed for the arising linear systems. Finally, for large-scale problems towards practical applications, multiscale or (non-intrusive) global-local approaches become important to keep the computational cost reasonable [28]. Therein, local problems contain the high-fidelity full nonlinear problem, which is coupled to a simpler (often

linear) global problem in the surrounding medium. Later, this idea was further extended to adaptive schemes [64], multilevel methods [2], extended/generalized finite elements for fracture [26], and thin-walled large deformations with phase-field [51]. More recently, due to the success of physics-informed neural networks, phase-field fracture numerical solutions are also solved with those methods [29, 30].

The starting point of the current work is the quasi-monolithic solution proposed in [32]. Therein a combined Newton method was designed in which the nonlinearities of constitutive laws and nonlinear coupling were combined with a primal-dual active set (PDAS) iteration to satisfy the crack irreversibility condition. First, in the current work the mathematical derivation of the primal-dual active set method is investigated in much more detail than in [32], by starting from a weak complementarity formulation. This provides (for the first time) a rigorous mathematical justification in terms of phase-field fracture formulations. The second objective is a significant improvement of the efficiency of the combined Newton method since in numerous simulations it was observed that Newton’s method converges fast, but the active set method needs many iterations, but often only a few degrees of freedom change. Sometimes, only the same degrees of freedom switch from active to non-active, which is known as cycling in the numerical optimization literature [20]. However, the physics of the solution does not change anymore significantly. To this end, we propose four test cases to find the impact of the active set method. Within these investigations, we analyze the role of a constant parameter inside the active set method. This constant was already mentioned in [37, 65, 68] and some theoretical statements were made, but it was not analyzed further. The third aim of this work is a bit specific. In [32], we introduced a linearization in terms of some extrapolation of (e.g., two) previous time-step solutions of the phase-field variable in the displacement equation in order to obtain a block-triangular Newton system matrix. This procedure results into an extremely robust nonlinear and linear numerical solution in which the linear system can be preconditioned with algebraic multigrid [33, 34] or geometric multigrid methods [40]. However, introducing such a linearization results into a temporal discretization error. For stationary or slowly growing fractures, this discretization error is sufficiently small. However, the error becomes significant the faster the fracture grows; see e.g., [76]. In order to reduce this temporal discretization error, one approach, proposed in [78], and further tested in [49], is to apply an additional iteration on the current time-step solution. Thus, we shall further investigate these additional iterations in terms of computational cost versus accuracy, as well as its behavior when combined with adaptive mesh refinement.

Gathering these developments together with the existing features in `pfm-cracks`, namely MPI (message passing interface) parallelization and predictor-corrector adaptive mesh refinement, a new final algorithm is designed by us in which the modified Newton method and the iteration on linearization (ItL) are realized and subsequently implemented. Various settings for stationary, nonstationary and two- and three-dimensional configurations are adopted to study the performance of our new algorithm.

mic framework. In the end, our aim is to substantiate a significant advancement of a parallel-adaptive phase-field fracture framework with a modern primal-dual active set strategy accounting for inequality constraints and iterating into the monolithic limit.

The outline of this paper is as follows: In Section 2, we describe the underlying setting of phase-field fracture. Then, we derive a complementarity system and obtain a series of intermediate mathematical results. In Section 3, our modified combined Newton scheme is introduced with four different cases. Then, in Section 4 an iteration is introduced, which iterates the linearized phase-field value into the monolithic limit. Afterwards, in Section 5 several numerical tests are conducted in order to study our novel algorithms for stationary, nonstationary two and three dimensional test cases. Our work is summarized in Section 6.

## 2 Problem formulation

### 2.1 Notations

This section introduces basic notations and the coupled variational inequality system (CVIS) and its discretized formulation, which is later used for simulations. The scalar-valued  $L^2$ -product on a sufficiently smooth, bounded domain  $G \subset \mathbb{R}^d$ ,  $d = 2, 3$  is denoted by

$$(x, y)_{L^2(G)} := \int_G x \cdot y \, dG,$$

whereas the vector-valued  $L^2$ -product is defined by

$$(X, Y)_{L^2(G)} := \int_G X : Y \, dG,$$

with the Frobenius product  $X : Y$  of two vectors  $X, Y$  and the material  $\Omega \subset \mathbb{R}^d$ , which is sufficiently smooth and bounded. If there is no subscript provided, the  $L^2$ -product over the whole domain  $\Omega$  is meant.

The Euler-Lagrange equations, arising from directional derivatives of an energy functional [25, 14] (pure elasticity), i.e., [59, 61] (pressured fractures in a monolithic setting), regularized with an Ambrosio-Tortorelli approximation [4, 5], consist of a displacement equation and the phase-field inequality and arise in a weak formulation. Consequently as solution variables, we have the displacement function  $u : \Omega \rightarrow \mathbb{R}^d$  and the phase-field function  $\varphi : \Omega \rightarrow [0, 1]$ . It is defined such that  $\varphi = 1$  in the intact part of the domain,  $\varphi = 0$  in the fully broken part of the domain and  $0 < \varphi < 1$  in the transition zone. The continuous-level solution sets are defined as

$$\mathcal{V} := H_0^1(\Omega), \quad \mathcal{K}^n := \{\psi \in \mathcal{W} \mid \psi - \varphi^{n-1} \leq 0 \text{ a.e. in } \Omega\}, \quad \text{where } \mathcal{W} := H^1(\Omega).$$

The convex set for the phase-field variable arises due to the crack irreversibility constraint  $\partial_t \varphi \leq 0$ , which reads in incremental form  $\varphi^n \leq \varphi^{n-1}$ , where  $\varphi^n := \varphi(t_n)$  and  $\varphi^{n-1} := \varphi(t_{n-1})$ . Here,  $t_n$  goes

from  $n = 0$  (initial condition) until  $n = N$  (end time condition) such that we have the incremental grid  $t_0, \dots, t_N$  and the step size  $k_n = t_n - t_{n-1}$ . However,  $k_n$  does only appear implicitly in the inequality constraint, and no time derivatives arise in the two governing problem statements, therefore, the resulting framework is of quasi-static fashion.

## 2.2 The phase-field fracture Euler-Lagrange equations

In this short section, we formulate a monolithic CVIS of phase-field fracture. First, we introduce constitutive laws and material parameters. We work with the classical stress tensor of linearized elasticity defined by

$$\sigma(u) = 2\mu e(u) + \lambda \operatorname{tr}(e(u))I,$$

with the Lamé parameters  $\mu > 0$ , and  $\lambda$  with  $3\lambda + 2\mu > 0$ , and the identity matrix  $I$ . The symmetric strain tensor  $e(u)$  is given by

$$e(u) := \frac{1}{2} (\nabla u + \nabla u^T).$$

Moreover, the critical energy release rate is denoted by  $G_C$  with  $G_C > 0$ .

Then, the Euler-Lagrange equations are given by [59, 61, 78]

**Problem 2.1.** (*Euler-Lagrange equations*) For some given initial value  $\varphi^0$  and for the incremental steps  $t_n$  with  $n = 1, \dots, N$ , find  $(u^n, \varphi^n) \in \mathcal{V} \times \mathcal{K}^n$  such that

$$(g(\varphi^n)\sigma(u^n), e(\psi^u)) + ((\varphi^n)^2 p^n, \operatorname{div} \psi^u) = 0 \quad \forall \psi^u \in \mathcal{V},$$

and

$$(1 - \kappa)(\varphi^n \sigma(u^n) : e(u^n), \psi^\varphi - \varphi^n) + 2(\varphi^n p^n \operatorname{div} u^n, \psi^\varphi - \varphi^n) + G_C \left( \frac{1}{\varepsilon} (1 - \varphi^n, \psi^\varphi - \varphi^n) + \varepsilon (\nabla \varphi^n, \nabla(\psi^\varphi - \varphi^n)) \right) \geq 0 \quad \forall \psi^\varphi \in \mathcal{K}^n \cap L^1(\Omega),$$

for a given pressure  $p^n \in L^1(\Omega)$  (Sneddon's test for pressured fractures [59, 61]) and  $p^n \equiv 0$  for fracture in pure elasticity.

Therein, the degradation function is given by  $g(\varphi^n) := (1 - \kappa)(\varphi^n)^2 + \kappa$ . The bulk regularization parameter  $\kappa$  is necessary to avoid irregularities in the system matrix. If the phase-field function  $\varphi$  is 0, we obtain zero-entries on the diagonal of the system matrix. To avoid this, we employ  $\kappa > 0$ . We have to ensure that  $\kappa$  is not too large since it yields a perturbation of the physics of the system, but it needs to be large enough to prevent irregularities. The second regularization parameter  $\varepsilon$  appears due to the Ambrosio Tortorelli approximation [4, 5]. The  $\Gamma$ -convergence theory, e.g [15], states on an energy-level that the regularized terms (under certain assumptions) converge to the underlying unregularized model as  $\varepsilon \rightarrow 0$ . A rigorous proof of pressurized phase-field fracture of the one dimensional case is done in [22], a proof in higher dimensions is established in [72]. For the discretized problem, we

also have to require  $h = o(\varepsilon)$  for the discretization parameter  $h$ . Finding an optimal setting for the regularization parameters  $\varepsilon$  and  $\kappa$ , which yields the best compromise between computational cost and  $\Gamma$ -convergence theory needs some work and is highly test dependent [43]. In practice, we usually must choose  $h < \varepsilon$  and often realized with  $\varepsilon = 2h$ .

### 2.3 A phase-field fracture formulation with degradation function linearization

Problem 2.1 has several nonlinearities, namely nonlinear coupling of variables in the displacement PDE (partial differential equation) and the phase-field inequality, while the inequality constraint introduces its own nonlinear behavior. A brief analysis of the coupling terms reveals that the nonlinear behavior in the displacement equation is more severe (being of quasi-linear type; for the definition of quasi-linear, we refer the reader to [23]) in comparison to the phase-field part, which is semi-linear only. Therefore, if linearizations are of interest, it is reasonable to address the quasi-linear part first. Indeed, the fully monolithic system is a big challenge to be solved [27, 77, 76, 44, 45, 49, 75, 31, 80]. We follow our prior work [32] and formulate a quasi-monolithic system in which we linearize  $(\varphi^n)^2$  by using known information about older incremental steps. In the first approach, we use an extrapolation for  $\varphi^n$  such that

$$\tilde{\varphi}^n := \tilde{\varphi}^n(\varphi^{n-1}, \varphi^{n-2}) = \varphi^{n-2} \frac{t_n - t_{n-1}}{t_{n-2} - t_{n-1}} + \varphi^{n-1} \frac{t_n - t_{n-2}}{t_{n-1} - t_{n-2}}.$$

In a second approach, we simply use the solution from the previous timestep such that

$$\tilde{\varphi}^n := \tilde{\varphi}^n(\varphi^{n-1}) = \varphi^{n-1}.$$

Furthermore, the stress can be split into a compressive and a tensile part such that the energy degradation only acts on the tensile stress, which introduces a third nonlinearity in the system. With these modifications, we obtain the following modified form of Problem 2.1.

**Problem 2.2.** (*Linearized Euler-Lagrange equations with stress-splitting*) For a given  $\varphi^0$  and for every incremental step  $t_n$  with  $n = 1, \dots, N$ , find  $U^n := \{u^n, \varphi^n\} \in \mathcal{V} \times \mathcal{K}^n$  such that it holds for  $\Phi := \{0, \varphi^n\} \in \mathcal{V} \times \mathcal{K}^n$

$$A(U^n)(\Psi - \Phi) \geq 0 \quad \forall \Psi := \{\psi^u, \psi^\varphi\} \in \mathcal{V} \times \mathcal{K}^n \cap L^1,$$

where  $A(U^n)(\Psi - \Phi)$  is defined as

$$\begin{aligned} A(U^n)(\Psi - \Phi) &:= (g(\tilde{\varphi}^n)\sigma^+(u^n), e(\psi^u)) + (\sigma^-(u^n), e(\psi^u)) + ((\tilde{\varphi}^n)^2 p^n, \operatorname{div} \psi^u) \\ &\quad + (1 - \kappa)(\varphi^n \sigma^+(u^n) : e(u^n), \psi^\varphi - \varphi^n) + 2(\varphi^n p^n \operatorname{div} u^n, \psi^\varphi - \varphi^n) \\ &\quad + G_C \left( \frac{1}{\varepsilon} (1 - \varphi^n, \psi^\varphi - \varphi^n) + \varepsilon (\nabla \varphi^n, \nabla(\psi^\varphi - \varphi^n)) \right), \end{aligned}$$

for a given pressure  $p^n \in L^1(\Omega)$ .

## 2.4 Derivation of a complementarity system

To treat the inequality in Problem 2.2, we employ a Lagrange multiplier  $\lambda^n$  by following [42]. Initially, this Lagrange parameter exists in the dual space of  $H^1(\Omega)$ , but in [74], the author states that  $\lambda^n \in L^2(\Omega)$  for single constraint variational inequality problems with solution variables in  $L^2(\Omega)$ . We assume that the argumentation can be transferred to Problem 2.2 and a rigorous proof is a goal for future work. With this, we can define

$$L^2(\Omega) := \{v \in L^2(\Omega) \mid v \leq 0 \quad \text{a.e. in } \Omega\},$$

and

$$\mathcal{N}_+ := \{\mu \in L^2(\Omega) \mid (\mu, v)_{L^2(\Omega)} \leq 0 \quad \forall v \in L^2(\Omega)\},$$

such that we can formulate a variational inequality system the classical  $L^2$  inner products and  $\mathcal{N}_+$  as solution set for the Lagrange multiplier  $\lambda^n$ .

**Problem 2.3.** *For a given  $\varphi^0$  and for the incremental steps  $t_n$  with  $n = 1, \dots, N$ , find  $U^n \in \mathcal{V} \times \mathcal{W}$  and  $\lambda^n \in \mathcal{N}_+$  such that*

$$\begin{aligned} A(U^n)(\Psi) + (\lambda^n, \psi^\varphi) &= 0 \quad \forall \Psi \in \mathcal{V} \times \mathcal{W} \cap L^1, \\ (\lambda^n - \xi, \varphi^n - \varphi^{n-1}) &\geq 0 \quad \forall \xi \in \mathcal{N}_+, \end{aligned}$$

where  $A(\cdot)(\cdot)$  is defined as before in Problem 2.2.

The numerical method, which is introduced in Section 3 to solve the inequality system, is designed to treat the variational inequality

$$(\lambda^n - \xi, \varphi^n - \varphi^{n-1}) \geq 0 \quad \forall \xi \in \mathcal{N}_+,$$

in a complementarity formulation. The following result states the equivalence of the previous variational inequality and a complementarity condition.

**Lemma 2.4.** *The variational inequality*

$$(\lambda^n - \xi, \varphi^n - \varphi^{n-1}) \geq 0 \quad \forall \xi \in \mathcal{N}_+, \tag{1}$$

can equivalently be formulated as a complementarity condition of the form

$$C(\varphi^n, \lambda^n) := \lambda^n - \max\{0, \lambda^n + c(\varphi^n - \varphi^{n-1})\} = 0, \tag{2}$$

for every  $c > 0$  and the max operation defined as

$$\max\{0, \lambda^n + c(\varphi^n - \varphi^{n-1})\} = \begin{cases} 0 & \text{in } \mathcal{I}, \\ \lambda^n + c(\varphi^n - \varphi^{n-1}) & \text{in } \mathcal{A}, \end{cases}$$

where the inactive set  $\mathcal{I} \subset \Omega$  and, the active set  $\mathcal{A} \subset \Omega$  are defined such that

$$\lambda^n + c(\varphi^n - \varphi^{n-1}) \leq 0 \text{ a.e. in } \mathcal{I},$$

$$\lambda^n + c(\varphi^n - \varphi^{n-1}) > 0 \text{ a.e. in } \mathcal{A}.$$

These two situations can be explained as follows. For  $\lambda^n = 0$  we are in the so-called inactive set, namely we solve the PDE part of phase-field. In  $\mathcal{A}$  the constraint is active, ‘we sit on the obstacle’, and we deal with  $\lambda^n > 0$ . Note, that  $\mathcal{A}$  and  $\mathcal{I}$  do not need to be connected, but note that  $\Omega \setminus \mathcal{I} \cup \mathcal{A}$  is a null set. The sets can be understood as unions of all nonempty subsets of  $\Omega$  with positive Lebesgue measure, on which the relations  $>$  or  $\leq$  are fulfilled almost everywhere.

*Proof.* The proof contains two major steps. Firstly, we prove the equivalence of (1) and a strong formulation of the form

$$\varphi^n - \varphi^{n-1} \leq 0 \quad \text{a.e. in } \Omega, \quad (3)$$

$$\lambda^n \geq 0 \quad \text{a.e. in } \Omega, \quad (4)$$

$$(\lambda^n, \varphi^n - \varphi^{n-1}) = 0. \quad (5)$$

Secondly, we show that (3)-(5) can be equivalently formulated as (2).

*Step 1:* ( $\Rightarrow$ ) Assume that (1) is satisfied. For (3), we assume the existence of a subset  $\mathcal{T} \subset \Omega$  with a positive Lebesgue measure such that it holds  $\varphi^n - \varphi^{n-1} > 0$  a.e. in  $\mathcal{T}$ . We define

$$\chi := \begin{cases} 2\lambda^n + 1 & \text{in } \mathcal{T}, \\ \lambda^n & \text{in } \Omega \setminus \mathcal{T}. \end{cases} \quad (6)$$

We have  $\chi \in \mathcal{N}_+$  and obtain that the variational inequality must hold for  $\mu = \chi$ . But it holds

$$\begin{aligned} (\lambda^n - \chi, \varphi^n - \varphi^{n-1}) &= (\lambda^n - \chi, \varphi^n - \varphi^{n-1})_{L^2(\mathcal{T})} + (\lambda^n - \chi, \varphi^n - \varphi^{n-1})_{L^2(\Omega \setminus \mathcal{T})} \\ &= (\lambda^n - 2\lambda^n - 1, \varphi^n - \varphi^{n-1})_{L^2(\mathcal{T})} + (\lambda^n - \lambda^n, \varphi^n - \varphi^{n-1})_{L^2(\Omega \setminus \mathcal{T})} \\ &= (-\lambda^n - 1, \varphi^n - \varphi^{n-1})_{L^2(\mathcal{T})} \\ &= (\lambda^n + 1, \varphi^{n-1} - \varphi^n)_{L^2(\mathcal{T})} < 0, \end{aligned}$$

since  $\varphi^{n-1} - \varphi^n < 0$  a.e. in  $\mathcal{T}$ ,  $\lambda^n \in \mathcal{N}_+$  and  $\lambda^n + 1 > 0$  a.e. in  $\Omega$ . Summarizing, we obtain

$$(\lambda^n - \chi, \varphi^n - \varphi^{n-1}) < 0,$$

which is a contradiction to the assumption that (1) is fulfilled. Thus, it must hold  $\varphi^n - \varphi^{n-1} \leq 0$  a.e. in  $\Omega$ . For (4), we assume  $\lambda^n < 0$  a.e. in a subset  $\mathcal{O} \subset \Omega$  with a positive Lebesgue measure. Then, we define

$$v := \begin{cases} \lambda^n & \text{in } \mathcal{O}, \\ 0 & \text{in } \Omega \setminus \mathcal{O}. \end{cases}$$



Then, it holds  $v \leq 0$  a.e. in  $\Omega$ . Thus, per definition of  $\mathcal{N}_+$  and since  $\lambda^n \in \mathcal{N}_+$ , it must hold that  $(\lambda^n, v) \leq 0$ . But we find

$$(\lambda^n, v) = \int_{\Omega} \lambda^n v \, dx = \int_{\mathcal{O}} \lambda^n v \, dx + \int_{\Omega \setminus \mathcal{O}} \lambda^n v \, dx = \int_{\mathcal{O}} \lambda^n \lambda^n \, dx + \int_{\Omega \setminus \mathcal{O}} \lambda^n \cdot 0 \, dx = \int_{\mathcal{O}} (\lambda^n)^2 \, dx > 0,$$

which is a contradiction. Thus, it must hold  $\lambda^n \geq 0$  a.e. in  $\Omega$ .

Lastly, we derive (5). We choose  $\xi = 0$ . Then, we have  $\xi \in \mathcal{N}_+$ . We obtain

$$(\lambda^n - 0, \varphi^n - \varphi^{n-1}) = (\lambda^n, \varphi^n - \varphi^{n-1}) \geq 0.$$

In a similar way, we can set  $\xi = 2\lambda^n$  to obtain

$$(\lambda^n - 2\lambda^n, \varphi^n - \varphi^{n-1}) = (-\lambda^n, \varphi^n - \varphi^{n-1}) = -(\lambda^n, \varphi^n - \varphi^{n-1}) \geq 0,$$

which yields  $(\lambda^n, \varphi^n - \varphi^{n-1}) \leq 0$ . Combining both inequalities finally leads to  $(\lambda^n, \varphi^n - \varphi^{n-1}) = 0$ .

( $\Leftarrow$ ) Now, we assume that (3)-(5) hold true. Firstly, (4) validates the choice of  $\mathcal{N}_+$  as solution space for  $\lambda^n$ . Let  $v \in L^2$  be arbitrary. Then, we obtain  $(\lambda^n, v) \leq 0$ , and consequently  $\lambda^n \in \mathcal{N}_+$ . Now, let  $\mu \in N$  be arbitrary. Due to (3), we have  $(\mu, \varphi^n - \varphi^{n-1}) \leq 0$ , and thus  $(-\mu, \varphi^n - \varphi^{n-1}) \geq 0$ . In combination with (5) we find

$$(\lambda^n - \mu, \varphi^n - \varphi^{n-1}) \geq 0.$$

Since  $\mu$  was chosen arbitrarily, we obtain (1).

*Step 2:* ( $\Rightarrow$ ) Let (3)-(5) be fulfilled. We define  $A, B \subset \Omega$  such that  $\varphi^n - \varphi^{n-1} < 0$  a.e. in  $A$  and  $\lambda^n > 0$  a.e. in  $B$ . As before, the sets  $A$  and  $B$  can be understood unions of all subsets on  $\Omega$  with positive Lebesgue measure, on which the relations  $>$  or  $\leq$  are fulfilled almost everywhere. We start by proving that  $A \cap B$  is a null set. For this, we assume that  $A \cap B$  has a positive Lebesgue measure. We find  $\lambda^n > 0$  a.e. in  $A \cap B$ , and  $\varphi^n - \varphi^{n-1} < 0$  a.e. in  $A \cap B$ . This yields

$$(\lambda^n, \varphi^n - \varphi^{n-1})_{\Omega} = (\lambda^n, \varphi^n - \varphi^{n-1})_{A \setminus B} + (\lambda^n, \varphi^n - \varphi^{n-1})_{\Omega \setminus (A \setminus B)} = (\lambda^n, \varphi^n - \varphi^{n-1})_{A \setminus B} < 0,$$

which is a contradiction to (5). Thus,  $A \cap B$  is a null set. In a next step, we prove that  $C(\varphi^n, \lambda^n) = 0$  a.e. in  $\Omega$ . It suffices to show that

$$C(\varphi^n, \lambda^n)|_{\mathcal{A}} = 0 \quad \text{a.e. in } \mathcal{A}, \quad C(\varphi^n, \lambda^n)|_{\mathcal{I}} = 0 \quad \text{a.e. in } \mathcal{I},$$

hold true. In  $\mathcal{A}$ , we have

$$\lambda^n \geq \lambda^n + c(\varphi^n - \varphi^{n-1}) > 0 \quad \text{a.e. in } \mathcal{A},$$

almost everywhere, which immediately yields  $\lambda^n > 0$  a.e. in  $\mathcal{A}$ . Due to previous findings, we consequently have  $\varphi^n - \varphi^{n-1} = 0$  a.e. in  $\mathcal{A}$ , and obtain

$$C(\varphi^n, \lambda^n)|_{\mathcal{A}} = \lambda^n - \max\{0, \lambda^n + c(\varphi^n - \varphi^{n-1})\} = \lambda^n - \lambda^n - c(\varphi^n - \varphi^{n-1}) = -c(\varphi^n - \varphi^{n-1}) = 0,$$

a.e. in  $\mathcal{A}$ . On  $\mathcal{I}$  we have

$$c(\varphi^n - \varphi^{n-1}) \leq \lambda^n + c(\varphi^n - \varphi^{n-1}) \leq 0 \quad \text{a.e. in } \mathcal{I},$$

which yields  $\varphi^n - \varphi^{n-1} \leq 0$  a.e. in  $\mathcal{I}$ . With the same argumentation as before, we conclude  $\lambda^n = 0$  a.e. in  $\mathcal{I}$  and obtain

$$C(\varphi^n, \lambda^n)|_{\mathcal{I}} = \lambda^n - \max\{0, \lambda^n + c(\varphi^n - \varphi^{n-1})\} = \lambda^n - 0 = 0,$$

a.e. in  $\mathcal{I}$ . Summarizing, (2) is fulfilled.

( $\Leftarrow$ ) Let (2) be fulfilled. As before, we have

$$\lambda^n + c(\varphi^n - \varphi^{n-1}) > 0 \quad \text{a.e. in } \mathcal{A}, \quad (7)$$

and

$$C(\varphi^n, \lambda^n) = \lambda^n - \lambda^n - c(\varphi^n - \varphi^{n-1}) = -c(\varphi^n - \varphi^{n-1}) = 0,$$

a.e. in  $\mathcal{A}$ , which is equivalent to  $\varphi^n - \varphi^{n-1} = 0$  a.e. in  $\mathcal{A}$ . Inserting this into (7) yields  $\lambda^n > 0$  a.e. in  $\mathcal{A}$ . On  $\mathcal{I}$  we have  $\lambda^n + c(\varphi^n - \varphi^{n-1}) \leq 0$  a.e. in  $\mathcal{I}$ , and thus, (2) yields  $\lambda^n = 0$  a.e. in  $\mathcal{I}$ . Thus, we find  $\varphi^n - \varphi^{n-1} \leq 0$  a.e. in  $\Omega$ . To obtain (5), we observe

$$(\lambda^n, \varphi^n - \varphi^{n-1}) = (\lambda^n, \varphi^n - \varphi^{n-1})_{\mathcal{A}} + (\lambda^n, \varphi^n - \varphi^{n-1})_{\mathcal{I}} = (\lambda^n, 0)_{\mathcal{A}} + (0, \varphi^n - \varphi^{n-1})_{\mathcal{I}} = 0.$$

With this, the proof is finished.  $\square$

In the following, the final system is stated and this is the starting point for the primal-dual active regularization.

**Problem 2.5.** (*Variational system with complementarity condition*) Given  $\varphi^0$  and for the incremental steps  $t_n$  with  $n = 1, \dots, N$ , find  $U^n = \{u^n, \varphi^n\} \in \mathcal{V} \times \mathcal{W}$  and  $\lambda^n \in \mathcal{N}_+$  such that

$$\begin{aligned} A(U^n)(\Psi) + (\lambda^n, \psi^\varphi) &= 0 \quad \forall \Psi = \{\psi^u, \psi^\varphi\} \in \mathcal{V} \times \mathcal{W} \cap L^1, \\ C(\varphi^n, \lambda^n) &= 0 \quad \text{a.e. in } \Omega, \end{aligned}$$

with  $A(U^n)(\Psi)$  and  $C(\varphi^n, \lambda^n)$  defined as before.

### 3 A modified combined nonlinear Newton-type algorithm

In this section, first, we recapitulate the principle numerical methods, which are used to solve the phase-field fracture problem introduced in Section 2 and implemented in `pfm-cracks` [34] based on the finite element library `deal.II` [7, 6]. The major computational features are an MPI parallelization (scalability tested on 1024 cores [33]), algebraic block-preconditioning using Trilinos [35] inside a GMRES (generalized minimal residuals) linear iterative solver, a primal-dual active method for

treating inequality constraints, and predictor-corrector mesh adaptivity by choosing a given small regularization parameter  $\varepsilon$  while guaranteeing  $h < \varepsilon$ , where  $h$  is the local mesh size.

In the following two sections, we perform two improvements. The first modification enhances the performance of the primal-dual active set method by adjusting the constant  $c$  introduced in (2). With the second modification, we improve the accuracy in time by updating the linearization term  $\tilde{\varphi}$  until convergence (into the monolithic limit) within one incremental step. The resulting final algorithm is then implemented in `pfm-cracks` and constitutes an extension to existing published work.

### 3.1 Newton's method

In each incremental step, the first equation of Problem 2.5 can be solved via a Newton method. Considering incremental step  $n$ , we seek for  $U^n := \{u^n, \varphi^n\} \in \mathcal{V} \times \mathcal{W}$  and  $\lambda^n \in \mathcal{N}_+$ . The solution  $U^n$  is found via iterating over  $k = 1, 2, 3, \dots$  until convergence, such that

$$A^0(U^{n,k})(\delta U^{n,k+1}, \Psi) + (\lambda^{n,k}, \psi^\varphi) = -A(U^{n,k})(\Psi) \quad \forall \Psi \in \mathcal{V} \times \mathcal{W}$$

with respect to

$$C(\varphi^{n,k} + \delta\varphi^{n,k+1}, \lambda^{n,k}) = 0 \quad \text{a.e. in } \Omega,$$

for the update  $\delta U^{n,k+1}$  and the Lagrange multiplier  $\lambda^{n,k+1}$  and updating via

$$U^{n,k+1} = U^{n,k} + \delta U^{n,k+1}.$$

The Jacobian  $A^0(U^{n,k})(\delta U^{n,k+1}, \Phi)$  is given by

$$\begin{aligned} A^0(U^{n,k})(\delta U^{n,k+1}, \Psi) &= \left( g(\tilde{\varphi}^n) \sigma^+(\delta u^{n,k+1}), e(\psi^u) \right) + \left( \sigma^+(\delta u^{n,k+1}), e(\psi^u) \right) \\ &\quad + (1 - \kappa) \left( \delta\varphi^{n,k+1} \sigma^+(u^{n,k}) : e(u^{n,k}) + 2\varphi^{n,k} \sigma^+(\delta u^{n,k+1}) : e(u^{n,k}), \psi^\varphi \right) \\ &\quad + 2p \left( \delta\varphi^{n,k+1} \operatorname{div} u^{n,k} + \varphi^{n,k} \operatorname{div} \delta u^{n,k+1}, \psi^\varphi \right) \\ &\quad + G_C \left( \frac{1}{\varepsilon} (\delta\varphi^{n,k+1}, \psi^\varphi) + \varepsilon (\nabla \delta\varphi^{n,k+1}, \nabla \psi^\varphi) \right), \end{aligned}$$

and  $A(U^{n,k})(\Phi)$  is defined as before. To treat the complementarity condition, we introduce the primal-dual active set method.

### 3.2 The primal-dual active set method

The primal-dual active set method (PDAS), introduced for constrained inequality systems in [8, 9, 38, 39], and shown under certain assumptions to be a semi-smooth Newton method [36], and applied on the phase-field fracture model in [32], is based on considerations made in Section 2. The idea is to split the domain into two subdomains in each incremental step  $n$ . On one subdomain, the inactive set  $\mathcal{I}^n$ , the inequality constraint  $\varphi^n - \varphi^{n-1} \leq 0$  is fulfilled strictly. On the other subdomain, the active set  $\mathcal{A}^n$ , it holds  $\varphi^n - \varphi^{n-1} = 0$ . A priori, these two sets are not known but combined

with the previously introduced Newton method, we obtain a prediction algorithm. Based on the complementarity condition, i.e., (2)

$$C(\varphi^{n,k} + \delta\varphi^{n,k+1}, \lambda^{n,k}) = 0,$$

we want to determine the active set  $\mathcal{A}^{n,k}$  and the inactive set  $\mathcal{I}^{n,k}$  such that

$$\lambda^{n,k} + c(\varphi^{n,k} - \varphi^{n-1}) > 0 \quad \text{a.e. in } \mathcal{A}^{n,k}, \quad \lambda^{n,k} + c(\varphi^{n,k} - \varphi^{n-1}) \leq 0 \quad \text{a.e. in } \mathcal{I}^{n,k}, \quad (8)$$

and iterate until the active set does not change within two consecutive Newton iterations. As before,  $\mathcal{A}^n$  can be understood as the union of all subsets of  $\Omega$  on which  $\lambda^n + c(\varphi^n - \varphi^{n-1}) > 0$  is fulfilled almost everywhere. The inactive set  $\mathcal{I}^n$  is then the complement of  $\mathcal{A}^n$  with respect to  $\Omega$ . If  $\mathcal{A}^n$  and  $\mathcal{I}^n$  are known, we can set  $\lambda^n = 0$  on  $\mathcal{I}^n$ , see Lemma 2.4, and treat the problem as an unconstrained problem. On  $\mathcal{A}^n$ , we set  $\varphi^n = \varphi^{n-1}$  and there is nothing to do (for the phase-field). The resulting scheme is given in Algorithm 1.

---

**Algorithm 1** (Primal-dual active set method)

---

- 1: Set iteration index  $k = 0$
- 2: **while**  $\mathcal{A}^{n,k} \neq \mathcal{A}^{n,k+1}$  **do**
- 3:     Determine the active set  $\mathcal{A}^{n,k}$  and inactive set  $\mathcal{I}^{n,k}$  with (8)
- 4:     Find  $\delta U^{n,k+1} \in \mathcal{V} \times \mathcal{W}$  and  $\lambda^{n,k+1} \in \mathcal{N}_+$  with solving

$$\begin{aligned} A^0(U^{n,k})(\delta U^{n,k+1}, \Phi) + (\lambda^{n,k+1}, \psi) &= -A(U^{n,k})(\Phi), \quad \forall \Phi := \{v, \psi\} \in \mathcal{V} \times \mathcal{W}, \\ \delta\varphi^{n,k+1} &= 0 \quad \text{on } \mathcal{A}^k, \\ \lambda^{n,k+1} &= 0 \quad \text{on } \mathcal{I}^k. \end{aligned}$$

- 5:     Update the solution to obtain  $U^{n,k+1}$  via

$$U^{n,k+1} = U^{n,k} + \delta U^{n,k+1}.$$

- 6:     Update iteration index  $k = k + 1$
  - 7: **end while**
- 

### 3.3 Discretization

We discretize Problem 2.5 using a finite element method with bilinear (2d) or trilinear (3d) elements  $Q_c^1$  [19] for both, the displacement function and the phase-field function. The discrete function spaces

read

$$\begin{aligned}\mathcal{V}_h &:= \left\{ u_h \in \mathcal{V}, u_h|_K \in [Q_1^c(K)]^d, \quad \forall K \in \mathcal{T}_h \right\}, \\ \mathcal{W}_h &:= \left\{ \varphi_h \in \mathcal{W}, \varphi_h|_K \in Q_1^c(K), \quad \forall K \in \mathcal{T}_h \right\}, \\ \mathcal{N}_h &:= \left\{ \lambda_h \in \mathcal{N}_+, \lambda_h|_K \in Q_1^c(K), \quad \forall K \in \mathcal{T}_h \right\},\end{aligned}$$

where  $K \in \mathcal{T}_h$  is the finite element and  $\mathcal{T}_h$  denotes the decomposition of the domain  $\Omega$  into a mesh, e.g., [19]. The spatially discretized system is formulated as follows:

**Problem 3.1.** (*Discretized system with complementarity condition*) Given  $\varphi_h^0$  and for the incremental steps  $t_n$  with  $n = 1, \dots, N$ , find  $(u_h^n, \varphi_h^n, \lambda_h^n) \in \mathcal{V}_h \times \mathcal{W}_h \times \mathcal{N}_h$  such that

$$\begin{aligned}A(u_h^n, \varphi_h^n)(\Phi_h) + (\lambda_h^n, \psi_h) &= 0 \quad \forall \Phi_h := (v_h, \psi_h) \in \mathcal{V}_h \times \mathcal{W}_h, \\ C(\varphi_h^n, \lambda_h^n) &= 0 \quad \forall x \in \Omega,\end{aligned}$$

with  $A(u_h^n, \varphi_h^n)(v_h, \psi_h)$  and  $C(\varphi_h^n, \lambda_h^n)$  defined as before in Lemma 2.4 with the point-wise maximum operation.

The application of a Galerkin ansatz with primitive ansatz and test functions of the form

$$\begin{aligned}\Phi_{h,i} &= \begin{bmatrix} \chi_i^u \\ 0 \end{bmatrix} \quad \text{for } i = 1, \dots, N_u, \\ \Phi_{h,N_u+i} &= \begin{bmatrix} 0 \\ \chi_i^\varphi \end{bmatrix} \quad \text{for } i = 1, \dots, N_\varphi,\end{aligned}$$

where  $N_u$  is the number of degrees of freedom in  $u_h$  and  $N_\varphi$  is the number of degrees of freedom in  $\varphi_h$ , leads to a system of the form

$$\begin{bmatrix} M & B \\ B^T & 0 \end{bmatrix} \begin{bmatrix} \delta U_h^{n,k+1} \\ \lambda_h^{k+1} \end{bmatrix} = \begin{bmatrix} F \\ 0 \end{bmatrix},$$

where  $B$  is a mass matrix and  $M$  and  $F$  are given by

$$M = \begin{bmatrix} M^{uu} & M^{u\varphi} \\ M^{\varphi u} & M^{\varphi\varphi} \end{bmatrix}, \quad F = \begin{bmatrix} F^u \\ F^\varphi \end{bmatrix},$$

with the block entries

$$\begin{aligned}
M_{ij}^{uu} &= (g(\tilde{\varphi}^n)\sigma^+(\chi_j^u), e(\chi_i^u)) + (\sigma^-(\chi_j^u), e(\chi_i^u)), \\
M_{ij}^{\varphi u} &= 2(1 - \kappa) \left( \varphi_h^{n,k} \sigma^+(\chi_j^u) : e(u_h^{n,k}), \chi_i^\varphi \right) + 2p \left( \varphi_h^{n,k} \operatorname{div}(\chi_j^u), \chi_i^\varphi \right), \\
M_{ij}^{u\varphi} &= 0, \\
M_{ij}^{\varphi\varphi} &= (1 - \kappa) \left( \sigma^+(u_h^{n,k}) : e(u_h^{n,k})\chi_j^\varphi, \chi_i^\varphi \right) + 2p \left( \operatorname{div}(u_h^{n,k})\chi_j^\varphi, \chi_i^\varphi \right) \\
&\quad + G_C \left( \frac{1}{\varepsilon} \left( \chi_j^\varphi, \chi_i^\varphi \right) + \varepsilon \left( \nabla \chi_j^\varphi, \nabla \chi_i^\varphi \right) \right),
\end{aligned}$$

and

$$\begin{aligned}
F_{ij}^u &= -A(U_h^{n,k})(\chi_i^u) = - \left( [(1 - \kappa)(\tilde{\varphi}_h^n)^2 + \kappa] \sigma^+(u_h^{n,k}), e(\chi_i^u) \right) - \left( \sigma^-(u_h^{n,k}), e(\chi_i^u) \right) \\
&\quad - \left( (\tilde{\varphi}_h^n)^2 p, \operatorname{div}(\chi_i^u) \right), \\
F_{ij}^\varphi &= -A(U_h^{n,k})(\chi_i^\varphi) = -(1 - \kappa) \left( \varphi_h^{n,k} \sigma^+(u_h^{n,k}) : e(u_h^{n,k}), \chi_i^\varphi \right) - 2 \left( \varphi_h^{n,k} p \operatorname{div}(u_h^{n,k}), \chi_i^\varphi \right) \\
&\quad - G_C \left( \frac{1}{\varepsilon} \left( 1 - \varphi_h^{n,k}, \chi_i^\varphi \right) + \varepsilon \left( \nabla \varphi_h^{n,k}, \nabla \chi_i^\varphi \right) \right).
\end{aligned}$$

We notice that the block  $M_{ij}^{u\varphi}$  is zero due to the previously applied linearization in  $\varphi$  in the displacement equation in Problem 2.2. Consequently, in the Newton system matrix, the corresponding directional derivative vanishes and it holds  $M_{ij}^{u\varphi} = 0$ . The main purpose is a robust nonlinear and linear solution; see also Remark 3.2.

Since the  $u_h^{n,k}$ ,  $\varphi_h^{n,k}$ ,  $\lambda_h^{n,k}$  are element-wise of polynomial structure, we can compute the active and inactive set point-wise:

$$\begin{aligned}
\mathcal{A}^{n,k} &= \left\{ x \mid \lambda_h^{n,k}(x) + c(\varphi_h^{n,k}(x) - \varphi_h^{n-1}(x)) > 0 \right\}, \\
\mathcal{I}^{n,k} &= \left\{ x \mid \lambda_h^{n,k}(x) + c(\varphi_h^{n,k}(x) - \varphi_h^{n-1}(x)) \leq 0 \right\}.
\end{aligned}$$

Given the fully discretized system, we can formulate the primal-dual active set method as it is implemented in `pfm-cracks` in Algorithm 2.

**Remark 3.2.** *In line 8, the reduced linear system is solved with a GMRES (generalized minimal residual) method [66] and algebraic multigrid preconditioning (AMG) [35]. In this work, the implementation as it is from `pfm-cracks` [34] is utilized. In our numerical tests (Section 5), we observe in all simulations between 10 – 40 linear iterations. This is in agreement with the results obtained in [33][Table 1]. The main reason for the excellent performance is twofold. First, it is the triangular block structure of  $\tilde{M}$  due to the zero block  $M_{ij}^{u\varphi}$  as previously discussed. Second, the diagonal terms in  $\tilde{M}$  are of elliptic type, which is well-known that multigrid methods perform very well.*

---

**Algorithm 2** (Primal-dual active set method with backtracking line search)

---

- 1: Set iteration index  $k = 0$
  - 2: **while**  $(\mathcal{A}^{n,k-1} \neq \mathcal{A}^{n,k})$  **or**  $(\tilde{R}(U_h^{n,k}) > \text{TOL}_N)$  **do**
  - 3:   Assemble the residual  $R(U_h^{n,k})$
  - 4:   Compute the active set  $\mathcal{A}^{n,k} = \left\{ x_i \mid [B]_{ii}^{-1} [R(U_h^{n,k})]_i + c(\varphi_{h,i}^{n,k} - \varphi_{h,i}^{n-1}) > 0 \right\}$
  - 5:   Set  $\varphi_h^{n,k} = \varphi_h^{n-1}$  on  $\mathcal{A}^{n,k}$
  - 6:   Assemble the system matrix  $M$  (Newton Jacobian) and the right-hand side  $F = R(U_h^{n,k})$
  - 7:   Eliminate rows/columns in  $\mathcal{A}^{n,k}$  from  $M$  and  $F$  to obtain  $\tilde{M}$  and  $\tilde{F} = \tilde{R}(U_h^{n,k})$
  - 8:   Solve the linear system  $\tilde{M}\delta U_h^{n,k+1} = \tilde{F}$  with GMRES and AMG preconditioner [34]
  - 9:   Choose maximum number of line search iterations  $l_{\max}$
  - 10:   Choose line search damping parameter  $0 < \omega \leq 1$
  - 11:   **for**  $l = 1 : l_{\max}$  **do**
  - 12:     Update the solution with  $U_h^{n,k+1} = U_h^{n,k} + \delta U_h^{n,k+1}$
  - 13:     Assemble the new residual  $\tilde{R}(U_h^{n,k+1})$
  - 14:     **if**  $\|\tilde{R}(U_h^{n,k+1})\|_2 < \|\tilde{R}(U_h^{n,k})\|_2$  **then**
  - 15:       **break**
  - 16:     **else**
  - 17:       Adjust the Newton update with  $\delta U_h^{n,k+1} := \omega^l \delta U_h^{n,k+1}$
  - 18:     **end if**
  - 19:   **end for**
  - 20:   Update iteration index  $k = k + 1$
  - 21: **end while**
- 

**Remark 3.3.** *The lines 9-19 describe a classical backtracking line search algorithm, where the Newton update is damped with a damping parameter  $\omega \in (0, 1]$ , if the updated solution  $U_h^{n,k+1} = U_h^{n,k} + \delta U_h^{n,k+1}$  does not reduce the residual norm. In all experiments in Section 5, we use  $l_{\max} = 10$  and  $\omega = 0.6$ .*

**Remark 3.4.** *Note that we deal with two systems of equations in Algorithm 2: the global nonlinear system and the reduced linear system. The nonlinear system consists of the matrix  $M$  and the right-hand-side  $F$ . The reduced linear system, defined by the matrix  $\tilde{M}$  and  $\tilde{F}$  only contains the equations of the nonlinear system, which belong to the inactive set. The residual of the full nonlinear system is then given by  $R$  whereas  $\tilde{R}$  denotes the residual of the reduced linear system. From an implementation point of view, this is realized by setting constraints to the system such that we enforce the phase-field to remain the same on the active degrees of freedom.*

### 3.4 Modified combined Newton active set algorithms

This section is dedicated to presenting adjustments to the primal-dual active set method based on an analysis of the active set constant  $c > 0$  (see again Lemma 2.4 and Algorithm 1). In [41], the authors prove for an obstacle problem that the primal-dual active set converges for any sufficiently large  $c > 0$ . Furthermore, they point out that  $c$  only influences the first active set iteration in theory. Similar observations were made in [37, 65, 68]. The authors state on the one hand that a constant  $c$  of magnitude around the Youngs modulus is reasonable from an engineer's perspective, while they also point out on the other hand, that different settings for  $c$  do not affect the solution but only the algorithmic performance. These results are a motivation to further investigate the influence of  $c$  for our primal-dual active set phase-field fracture formulation. We start by pointing out the bottleneck of the above described primal-dual active set algorithm. Specifically on fine meshes, we often run into convergence issues of the active set, whereas the residual converges comparably fast (see e.g., [32][Fig. 14]).

#### 3.4.1 Investigation of the active set constant $c$

In the following, our objective is to illustrate the influence of the active set constant  $c$  and how to adjust it to reduce the number of active set iterations. To this end, we begin with an investigation of the role of the active set constant  $c$  in the algorithm. It is involved in the classification of the active set  $\mathcal{A}^k$  as a degree of freedom  $x_i$  is classified as active (in iteration  $k$  within the current incremental step), if

$$\lambda_{h,i}^k + c(\varphi_{h,i}^k - \varphi_{h,i}^{\text{old}}) > 0,$$

where  $\varphi_{h,i}^{\text{old}}$  is the value of the phase field solution of the previous incremental step at degree of freedom  $i$ . We identify nine different situations, depending on the sign of  $\lambda_{h,i}^k$  and  $(\varphi_{h,i}^k - \varphi_{h,i}^{\text{old}})$ :

1.  $\varphi_{h,i}^k - \varphi_{h,i}^{\text{old}} = 0$ , and  $\lambda_{h,i}^k > 0 \Rightarrow \varphi_{h,i}^k = \varphi_{h,i}^{\text{old}}$ ,  $\delta\varphi_{h,i}^{k+1} = 0$  and  $\lambda_{h,i}^{k+1} = B_{ii}^{-1}F_i$
2.  $\varphi_{h,i}^k - \varphi_{h,i}^{\text{old}} = 0$ , and  $\lambda_{h,i}^k = 0 \Rightarrow \delta\varphi_{h,i}^{k+1}$  as solution of the system and  $\lambda_{h,i}^{k+1} = 0$
3.  $\varphi_{h,i}^k - \varphi_{h,i}^{\text{old}} = 0$ , and  $\lambda_{h,i}^k < 0 \Rightarrow \varphi_{h,i}^k = \varphi_{h,i}^{\text{old}}$ ,  $\delta\varphi_{h,i}^{k+1} = 0$  and  $\lambda_{h,i}^{k+1} = B_{ii}^{-1}F_i$
4.  $\varphi_{h,i}^k - \varphi_{h,i}^{\text{old}} > 0$ , and  $\lambda_{h,i}^k > 0 \Rightarrow \delta\varphi_{h,i}^{k+1} = 0$  and  $\lambda_{h,i}^{k+1} = B_{ii}^{-1}F_i$
5.  $\varphi_{h,i}^k - \varphi_{h,i}^{\text{old}} > 0$ , and  $\lambda_{h,i}^k = 0 \Rightarrow \varphi_{h,i}^k = \varphi_{h,i}^{\text{old}}$ ,  $\delta\varphi_{h,i}^{k+1} = 0$  and  $\lambda_{h,i}^{k+1} = B_{ii}^{-1}F_i$
6.  $\varphi_{h,i}^k - \varphi_{h,i}^{\text{old}} > 0$ , and  $\lambda_{h,i}^k < 0 \Rightarrow \begin{cases} \varphi_{h,i}^k = \varphi_{h,i}^{\text{old}}, \delta\varphi_{h,i}^{k+1} = 0, \lambda_{h,i}^{k+1} = B_{ii}^{-1}F_i & \text{if } |\lambda_{h,i}^k| < c(\varphi_{h,i}^k - \varphi_{h,i}^{\text{old}}), \\ \delta\varphi_{h,i}^{k+1} \text{ as solution, } \lambda_{h,i}^{k+1} = 0 & \text{otherwise.} \end{cases}$
7.  $\varphi_{h,i}^k - \varphi_{h,i}^{\text{old}} < 0$ , and  $\lambda_{h,i}^k > 0 \Rightarrow \begin{cases} \delta\varphi_{h,i}^{k+1} \text{ as solution, } \lambda_{h,i}^{k+1} = 0 & \text{if } \lambda_{h,i}^k \leq |c(\varphi_{h,i}^k - \varphi_{h,i}^{\text{old}})| \\ \varphi_{h,i}^k = \varphi_{h,i}^{\text{old}}, \delta\varphi_{h,i}^{k+1} = 0, \lambda_{h,i}^{k+1} = B_{ii}^{-1}F_i & \text{otherwise} \end{cases}$



8.  $\varphi_{h,i}^k - \varphi_{h,i}^{\text{old}} < 0$ , and  $\lambda_{h,i}^k = 0 \Rightarrow \delta\varphi_{h,i}^{k+1}$  as solution,  $\lambda_{h,i}^{k+1} = 0$
9.  $\varphi_{h,i}^k - \varphi_{h,i}^{\text{old}} < 0$ , and  $\lambda_{h,i}^k < 0 \Rightarrow \delta\varphi_{h,i}^{k+1}$  as solution,  $\lambda_{h,i}^{k+1} = 0$ .

We observe that the active set constant  $c$  only has an influence on the classification when  $\lambda_{h,i}^k$  and  $\varphi_{h,i}^k - \varphi_{h,i}^{\text{old}}$  have different signs. In situation No. 6,  $\varphi_{h,i}^k$  shows crack healing behaviour, thus we do not want to accept it as a solution and set it to  $\varphi_{h,i}^{\text{old}}$ . We achieve this, if

$$|\lambda_{h,i}^k| < c(\varphi_{h,i}^k - \varphi_{h,i}^{\text{old}}),$$

i.e.

$$\frac{|\lambda_{h,i}^k|}{(\varphi_{h,i}^k - \varphi_{h,i}^{\text{old}})} < c.$$

In situation No. 7, we do not violate the constraint with the solution of the  $k$ th iteration, thus, we still want to classify this degree of freedom as inactive. This can be achieved via

$$\lambda_{h,i}^k \leq c|(\varphi_{h,i}^k - \varphi_{h,i}^{\text{old}})|,$$

i.e.

$$\frac{\lambda_{h,i}^k}{|(\varphi_{h,i}^k - \varphi_{h,i}^{\text{old}})|} < c.$$

Summarizing, we can formulate a condition for  $c$ :

$$\left| \frac{\lambda_{h,i}^k}{(\varphi_{h,i}^k - \varphi_{h,i}^{\text{old}})} \right| < c.$$

Thus, any  $c$  larger than the lower bound is sufficiently large.

### 3.4.2 Proposed adjustments and definition of four cases

In the following, we propose four different cases for implementing the Newton active set algorithm. The basis for these cases is Algorithm 2. For better readability and since the concepts are the same in each incremental step, we drop the incremental index  $n$ . Both stopping criteria, i.e., if not stated otherwise, require the active set to converge and the residual-norm to fall below a certain tolerance. For our adjustment, we choose

$$c = c^k := 2 \left| \frac{\lambda_{h,i}^k}{(\varphi_{h,i}^k - \varphi_{h,i}^{\text{old}})} \right|,$$

thus, in contrast to before,  $c$  changes in every Newton iteration. This could be avoided by iterating until convergence, saving the largest  $c^k$  and then restarting the iteration. But this is an unnecessary computational cost and in our opinion, a varying  $c^k$  does not lead to any conflicts. In Section 5, we will perform several experiments to observe the performance boost of this adjustment. Based on the previous findings, we suggest four different cases:

- **Case 1:** We iterate as long as the active set does not change within 2 iterations with a constant  $c = 10E$ , where  $E$  is Young's modulus. Let  $k$  be the iteration index and  $\mathcal{A}^k$  the active set of iteration  $k$ , we stop, when  $\mathcal{A}^k = \mathcal{A}^{k+1}$  and  $\|\tilde{R}(U_h^{k+1})\|_2 < \text{TOL}_N$ .
- **Case 2:** The classification of active/inactive set proceeds as in **Case 1**, but with the modified  $c$  set as

$$c = c^k = 2 \left| \frac{\lambda_{h,i}^k}{(\varphi_{h,i}^k - \varphi_{h,i}^{\text{old}})} \right|.$$

Apart from this, everything is similar to Algorithm 2 including the stopping criteria: we stop, when  $\mathcal{A}^k = \mathcal{A}^{k+1}$  and  $\|\tilde{R}(U_h^{k+1})\|_2 < \text{TOL}_N$ .

- **Case 3:** The classification of the active/inactive set proceeds as in **Case 1** with  $c = 10E$ . But in this case, we weaken the active set stopping criterion, i.e. we do not enforce  $\mathcal{A}^k = \mathcal{A}^{k+1}$  for termination anymore. Instead, we perform as much Newton active set iterations as needed to achieve  $\|\tilde{R}(U_h^{k+1})\|_2 < \text{TOL}_N$ . When this is fulfilled, we only perform 10 more Newton active set iterations until we stop. The number 10 is chosen heuristically based on our experiences in this paper. It is a compromise between sufficiently many iterations to guess that we may have converged and computational cost by not adding too many additional iterations.
- **Case 4:** The classification of the active/inactive set proceeds as in **Case 1** with  $c = 10E$ . But in this case, we completely omit the active set stopping criteria. This means, we do not require  $\mathcal{A}^k = \mathcal{A}^{k+1}$  but stop immediately as soon as  $\|\tilde{R}(U_h^{k+1})\|_2 < \text{TOL}_N$  is reached.

## 4 Iteration on the linearization into the monolithic limit

Both introduced linearization strategies (Section 2.3) to treat the nonlinearity in the displacement equation come with limitations of the above model. They lead to so-called time-lagging behaviour (temporal/incremental discretization error), where the crack grows slower than physics of the governing model suggest; see for instance [76][Fig. 3]. Based on concepts developed in [78][Section 7.7.3], we employ an iteration on the linearization, such that the iteration converges into the monolithic limit. The idea is to employ an additional fixed-point iteration. In this fashion, we iterate until the  $L^2$ -difference between two consecutive iterative solutions is smaller than a predefined tolerance. This concept can be applied to both the extrapolation (ItE) and the linearization by using the solution from the previous incremental step (ItOTS); see again Section 2.3. For the former, numerical studies were already done in [49].

The main objective is to further investigate ItE in practice (since from a pure mathematical point of view the extrapolation is only heuristic since no regularity in time can be ensured since  $\partial_t \varphi$  is only a bounded measure [60][p. 1384, Theorem 1] shown for a decoupled formulation; but for extrapolation more regularity is required). For comparison, we utilize as well ItOTS. Along with these iterations

into the monolithic limit, a challenge is its combination with predictor-corrector adaptivity. In the predictor-corrector algorithm [32][Section 4] first a new crack path is predicted, and then solved again on the new mesh. Iterating on the new mesh into the monolithic limit may result into a previous under-estimation of the crack path, for which the predictor-corrector algorithm needs to be re-started, because the condition  $h < \varepsilon$  might be violated since the predicted refinement area was not large enough. Of course, this double iterations can become quite expensive and finally it is a compromise between two typical numerical demands, namely efficiency and accuracy.

Therefore, our recommendation is not that we must use the full algorithm in all various cases, it is rather a decision choice what is more important: very small internal length scales  $\varepsilon$  (thus predictor-corrector adaptivity is likely needed), overall accuracy of the solution, overall efficiency (including adaptivity and/or parallel computing).

In consequence, our newly proposed final Algorithm 3 includes the following iterations: The loop over the incremental steps, the iteration on the linearization, possible predictor-corrector adaptive mesh refinement iteration, the nonlinear Newton active set iteration and the linear solver iteration.

---

**Algorithm 3** (Quasi-monolithic solution algorithm including iteration on the linearization)

---

```
1: Setup the system ▷ initialize grid  $\mathcal{T}_h$ , parameters, etc.
2: Set  $\mathcal{T}_h^{\text{old}} = \mathcal{T}_h$ 
3: for  $n = 1, 2, \dots$  do ▷ timestep loop
4:   Set  $\text{changed}_{\text{mesh}} = \mathbf{true}$ 
5:   while ( $\text{changed}_{\text{mesh}}$ ) do ▷ adaptive predictor-corrector refinement
6:     Set  $\varphi_h^{n,1} = \varphi_h^{n,2}$  ▷ preparations for iteration on the linearization
7:     Set  $\varphi_h^{n,0} = \varphi_h^{n,1}$  ▷ preparations for iteration on the linearization
8:     Set  $j = 0$  ▷ index for iteration on the linearization
9:     while ( $\|\varphi_h^{n,j} - \varphi_h^{n,j-1}\|_2 \geq \text{TOL}_{\text{ItL}}$ ) or ( $j < 1$ ) do ▷ iteration on the linearization
10:      Compute the linearization  $\tilde{\varphi}_h^{n,j}$  ▷ compute the linearization (Section 2.3)
11:      Set  $j = j + 1$  ▷ update ItL index
12:      Solve system with PDAS to obtain  $\{u_h^{n,j}, \varphi_h^{n,j}\}$  ▷ Algorithm 2 with linearization in
assembly
13:     end while
14:     Refine the mesh to obtain new mesh  $\mathcal{T}_h^{\text{new}}$  ▷ predictor-corrector scheme [32]
15:     if  $\mathcal{T}_h^{\text{new}} = \mathcal{T}_h^{\text{old}}$  then ▷ Check whether mesh changed or not
16:       Set  $\text{changed}_{\text{mesh}} = \mathbf{false}$  ▷ If did not change, leave while loop
17:     else
18:       Set  $\mathcal{T}_h^{\text{old}} = \mathcal{T}_h^{\text{new}}$  ▷ Else, save current mesh and goto line 6
19:     end if
20:   end while
21: end for
```

---

## 5 Numerical examples

In this section, we propose several numerical tests for the previously introduced algorithms. In the first two examples, the Sneddon test in two and three dimensions, we compare the required Newton active set iterations for solving the problem for the four different cases (Section 3.4.2). Since these tests are steady-state, i.e. we have a non-growing fracture, the iteration on the linearization is not necessary and does not affect the solution. Thus, we only compute one linearization step. In these examples, we exclusively use the extrapolation.

In three other examples, where we face growing fractures, the time-lagging phenomenon due to the linearization can be observed very well. In these tests, we use the iteration on the linearization (ItL) until a certain tolerance is reached and compare the Newton iterations with and without ItL for both the iteration on the extrapolation (ItE) and the iteration via the previous incremental step solution (ItOTS). We also test the active set modifications from Section 3.4, but we did not observe significant differences between **Case 1** and **Case 2**. We assume, that the modification predominantly affects the number of active set iterations on very fine meshes (see Section 5.1 and Section 5.2). Thus, all results shown in Section 5.3 to 5.5 are obtained from **Case 2**.

### 5.1 Sneddon 2d

We consider a stationary benchmark test [67], where a constant pressure is applied in the inner of a pre-existing crack in the middle of a domain, and only the crack width varies. This test setup is motivated by Sneddon [70], and Sneddon and Lowegrub [71]. We restrict ourselves to a one dimensional fracture  $C$  on a two dimensional domain  $\Omega = (-10, 10)^2$  as depicted in Figure 1 on the left. The fracture is centered horizontally within  $\Omega$  and has a constant half crack length  $l_0 = 0.25$  and varying width. Precisely, the crack width corresponds to  $2h$ , where  $h$  is the minimal element diameter of the mesh. The mesh is pre-refined geometrically in the crack zone, as depicted exemplarily for one adaptive refinement step in Figure 1 on the right, where the crack zone is resolved with the smallest mesh size. The driving force is given by a constant pressure  $\rho = 10^{-3}$  Pa in the inner crack. The parameter setting is given in Table 1.

The spatial discretization parameter, i.e. the minimal element diameter, is set as

$$h = 0.022, 0.011, 0.0055, 0.0027, 0.0013.$$

The quantity of interest, called total crack volume (TCV), can be computed numerically via

$$\text{TCV} = \int_{\Omega} u(x, y) \nabla \varphi(x, y) d(x, y).$$

The analytical solution [71] is given by

$$\text{TCV}_{\text{ref}} = \frac{2\pi\rho l_0^2}{E^0}.$$

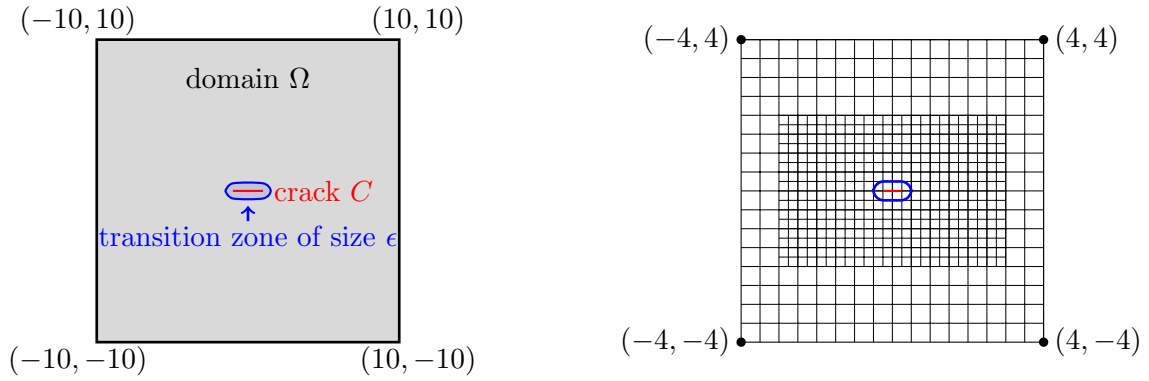


Figure 1: Left: geometry of the two dimensional Sneddon test. Right: zoom-in to the pre-refined crack zone in  $[-4, 4] \times [-4, 4]$  with two global refinement steps and one local refinement step (geometrically pre-refined).

Parameter	Definition	Value
$\Omega$	Domain	$(-10, 10)^2$
$h$	Diagonal cell diameter	test-dependent
$l_0$	Half crack length	0.25
$G_C$	Material toughness	1.0
$E$	Young's modulus	1.0
$\mu$	Lamé parameter	0.42
$\lambda$	Lamé parameter	0.28
$\nu$	Poisson's ratio	0.2
$p$	Applied pressure	$10^{-3}$
$\epsilon$	Bandwidth of the initial crack	$2h$
$\kappa$	Regularization parameter	$10^{-10}$
	Number of global refinements	2
	Number of local refinements	5, 6, 7, 8, 9
$TOL_N$	Tolerance outer Newton solver	$10^{-7}$
	Tolerance inner linear solver	$\mathbf{k}\tilde{R}(U_h^{n,k})\mathbf{k}_2 10^{-8}$

Table 1: The setting of the material and numerical parameters for the Sneddon 2d test.

The Figures 2 - 5 visualize the average active-set iterations required per time-step for **Case 1-Case 4** and  $h = 0.022, 0.011, 0.0055, 0.0027$ . We observe, that with a smaller  $h$ , the number of iterations can become comparatively large in **Case 1** in comparison to the other cases. We also ran a test with a minimal element diameter  $h = 0.0013$  which leads to around 40 million degrees of freedom. There, the Newton active set method did not achieve convergence within 500 Newton active set iterations with **Case 1** in the 2nd incremental step. In contrast, with the modified constant  $c$  from **Case 2**, the Newton method terminates within 46, 26, 18, 7 and 4 iterations to converge at each incremental step. With **Case 3** 10 – 11 Newton active set iterations are needed in each timestep on each refinement level. With **Case 4** only 1 iteration is needed. The latter shows that the Newton method only needs 1 iteration to converge, which underlines the assumption that the active set stopping criterion is indeed the reason for the slow convergence in **Case 1**. The speed-up coming along with **Case 3**, **Case 4** and especially **Case 2** has a noticeable impact in the computation time, which is summarized for all settings in Table 2. The speed-up of **Case 3** and **Case 4** must be treated with caution since we do not iterate until full convergence of the active set in these cases, which may lead to reduced accuracy.

	Total wallclock time j Sneddon 2d				
Case	$h = 0.022$ j 4 cores	$h = 0.011$ j 4 cores	$h = 0.0055$ j 16 cores	$h = 0.0027$ j 32 cores	$h = 0.0013$ j 64 cores
Case 1	587.983s	2243.164s	2275.481s	11682.962s	–
Case 2	161.765s	976.391s	784.019s	2590.394s	6562.554s
Case 3	117.775s	458.664s	572.438s	1228.499s	4132.350s
Case 4	22.833s	77.788s	87.405s	208.310s	940.686s

Table 2: Total wallclock time of the Sneddon 2d test for different refinement levels on different numbers of cores.

As it can be observed in Table 3, the error in the TCV is not affected, even though we completely ignore the active set stopping criterion (**Case 4**). But in this case, we may obtain a non-smooth phase-field solution. This phenomenon is depicted in Figure 6. The slight increase of the TCV error for  $h < 0.0055$  can be attributed to the fact that the analytical solution is based on an infinite domain. Thus, the solution does not converge to the exact solution for  $h \rightarrow 0$  since the domain-error due to the finite domain will become dominant if  $h$  is small enough, which is the case for  $h < 0.0055$ , as we assume. This phenomenon was further investigated in [33].

Lastly, a brief parallel study is conducted. The framework is parallelized with MPI. Since it is based on the `pfm-cracks` code [34], extensive scalability analyses can be found in [33]. We compare the CPU time for one representative incremental step for  $h = 0.022$  (168 609 degrees of freedom) computed on 1 core and 16 cores. On 1 core, the CPU time of one incremental step is 2386s (approx. 18h) and on 16 cores, the CPU time is 142s.

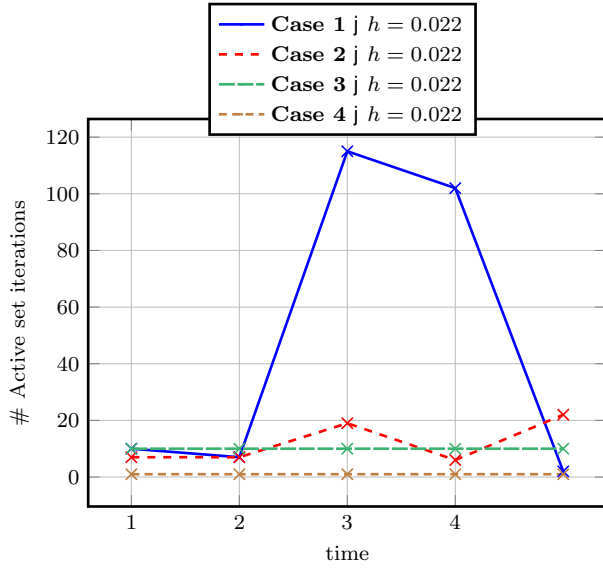


Figure 2: Number of active set iterations for **Case 1-Case 4** and  $h = 0.022$  in the Sneddon 2d test.

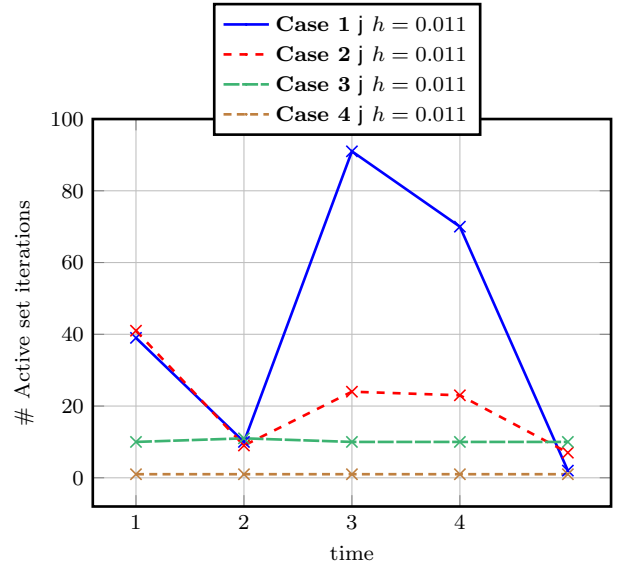


Figure 3: Number of active set iterations for **Case 1 to Case 4** and  $h = 0.011$  in the Sneddon 2d test.

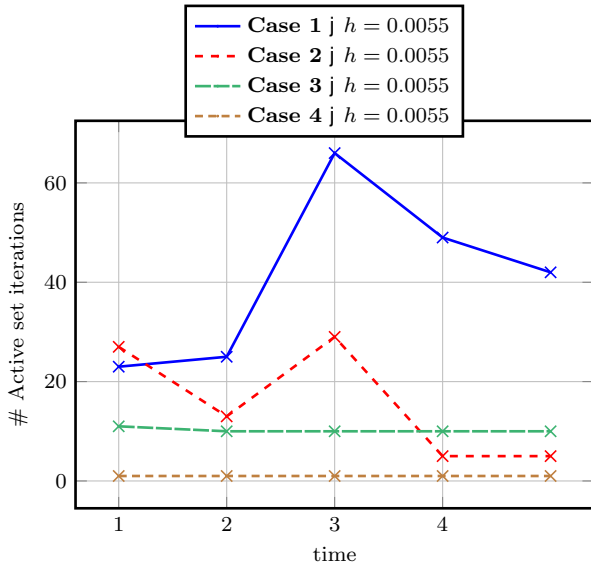


Figure 4: Number of active set iterations for **Case 1-Case 4** and  $h = 0.0055$  in the Sneddon 2d test.

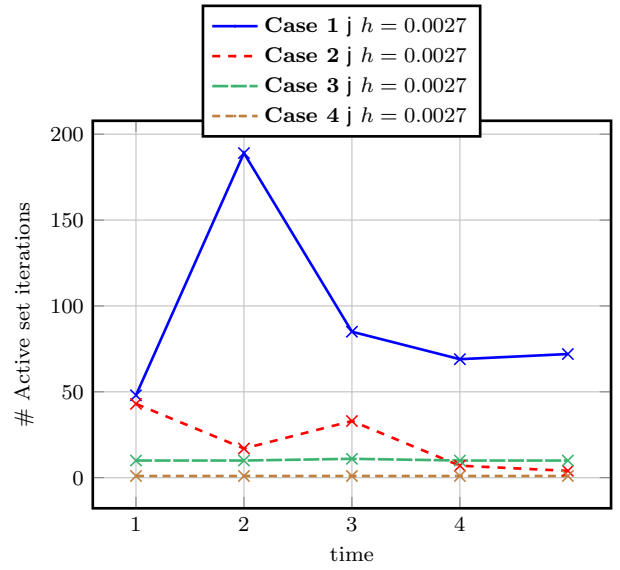


Figure 5: Number of active set iterations for **Case 1-Case 4** and  $h = 0.0027$  in the Sneddon 2d test.

Case	TCV error j Sneddon 2d				
	$h = 0.022$	$h = 0.011$	$h = 0.0055$	$h = 0.0027$	$h = 0.0013$
Case 1	0.000173649	3.72255e-05	3.03573e-05	6.45367e-05	–
Case 2	0.000173649	3.72255e-05	3.03573e-05	6.45367e-05	8.19169e-05
Case 3	0.000173649	3.72255e-05	3.03573e-05	6.45367e-05	8.19169e-05
Case 4	0.000173649	5.33208e-05	3.03573e-05	6.14307e-05	8.19169e-05

Table 3: Error in the TCV for different mesh size parameters and **Case 1 - Case 4**.





Figure 6: Visualization of the nonsmooth phase-field solution of the two dimensional Sneddon test with  $h = 0.011$  and **Case 4**. Red represents the fully intact part of the domain, blue the fully broken part and white stands for the transition zone.

## 5.2 Sneddon 3d

The Sneddon 3d test [71][Section 3.3] is the three dimensional equivalent of the Sneddon 2d test. We have a three dimensional cubic domain  $\Omega$  and a two dimensional penny-shaped fracture with a pressure acting in its center. As in Section 5.1, we compare the number of Newton iterations for **Case 1** - **Case 4**. The results for different mesh size parameters  $h = 1.732, 0.866, 0.433, 0.216$  are depicted in Figure 7 - Figure 10. On coarser grids, **Case 1** and **Case 2** perform very similarly, whereas on finer meshes, the benefit of **Case 2** is seen especially in the fourth incremental step. As assumed, **Case 4** yields the lowest number of active set iterations and **Case 3** yields a constant number of iterations of around 10 – 12 per incremental step.

Parameter	Definition	Value
$\Omega$	Domain	$(10, 10)^3$
$h$	Diagonal cell diameter	test-dependent
$r_0$	crack radius	1.0
$G_C$	Material toughness	1.0
$E$	Young's modulus	1.0
$\mu$	Lamé parameter	0.42
$\lambda$	Lamé parameter	0.28
$\nu$	Poisson's ratio	0.2
$p$	Applied pressure	$10^{-3}$
$\varepsilon$	Bandwidth of the initial crack	$2h$
$\kappa$	Regularization parameter	$10^{-10}h$
	Number of global refinements	1
	Number of local refinements	0, 1, 2, 3
$TOL_N$	Tolerance outer Newton solver	$10^{-7}$
	Tolerance inner linear solver	$\mathbf{k}\tilde{R}(U_h^{n,k})\mathbf{k}_2 10^{-8}$

Table 4: The setting of the material and numerical parameters used for the Sneddon 3d test.

We mention since the crack does not grow in Section 5.1 and Section 5.2 that there is numerically no

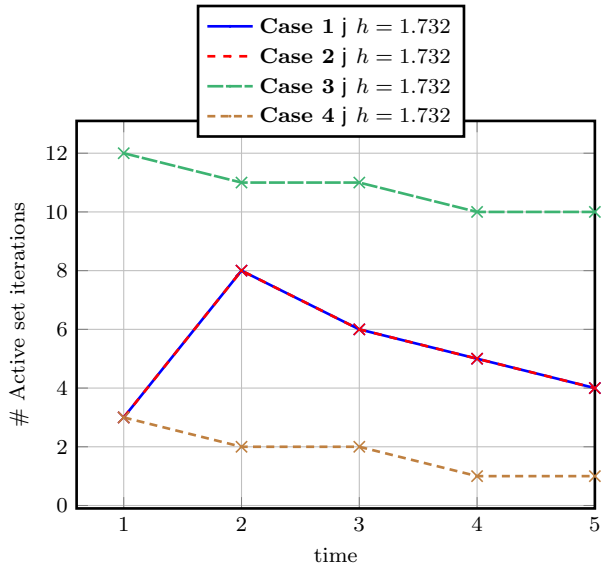


Figure 7: Number of active set iterations for **Case 1-Case 4** and  $h = 1.732$  for the Sneddon 3d test.

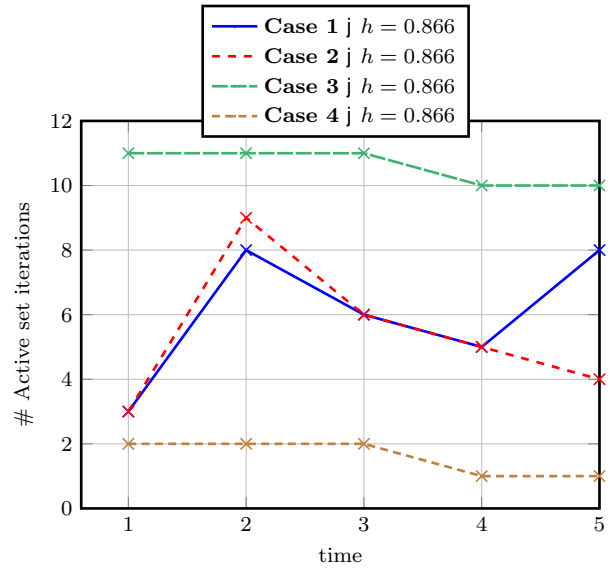


Figure 8: Number of active set iterations for **Case 1-Case 4** and  $h = 0.866$  for the Sneddon 3d test.

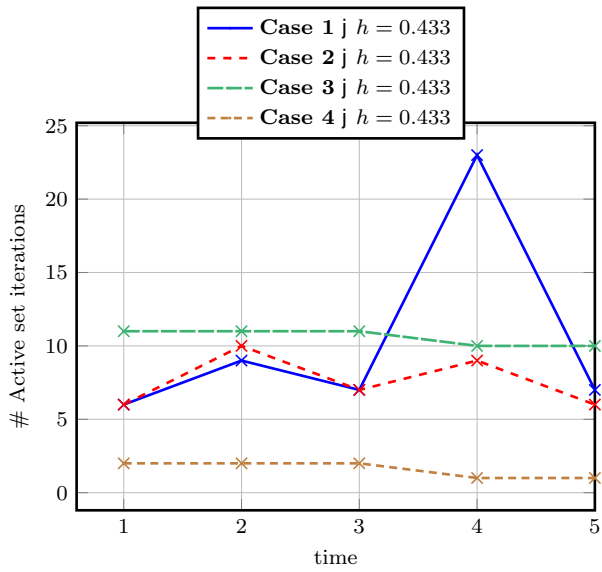


Figure 9: Number of active set iterations for **Case 1-Case 4** and  $h = 0.433$  for the Sneddon 3d test.

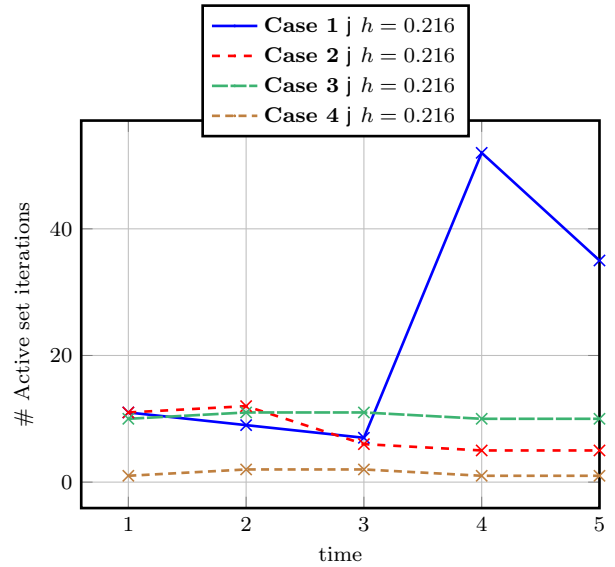


Figure 10: Number of active set iterations for **Case 1-Case 4** and  $h = 0.216$  for the Sneddon 3d test.

Case	TCV error j Sneddon 3d			
	$h = 1.732$	$h = 0.866$	$h = 0.433$	$h = 0.216$
Case 1	0.061265	0.0220069	0.00897784	0.00352026
Case 2	0.061265	0.0220069	0.00897784	0.00352026
Case 3	0.061265	0.0220069	0.00897784	0.00352026
Case 4	0.061265	0.0220069	0.00897606	0.00352025

Table 5: Error in the TCV of the 3 dimensional Sneddon test for different mesh size parameters and **Case 1 - Case 4**.

difference whether ItL is utilized or not. For this reason, we concentrate on the active set performance only. However, as in the two dimensional case, the reduction of the number of Newton iterations with **Case 2**, **Case 3** and **Case 4** leads to a significant speed-up, which can be observed by comparing the total wallclock times and is summarized in Table 6.

	Total wallclock time j Sneddon 3d			
Case	$h = 1.732$ j 32 cores	$h = 0.866$ j 48 cores	$h = 0.433$ j 128 cores	$h = 0.216$ j 128 cores
Case 1	19.669s	24.089s	267.847s	888.671s
Case 2	19.981s	21.836s	191.004s	637.236s
Case 3	36.249s	37.906s	322.549s	590.830s
Case 4	9.949s	10.580s	87.367s	162.499s

Table 6: Total wallclock time of the Sneddon 3d test for different refinement levels on different numbers of cores.

Finally, in this example, we test the parallel performance with  $h = 0.433$  by comparing the CPU time for one incremental step. On 1 core, 8889s (approx. 2.4h) were needed whereas the CPU time on 16 cores is 542s (approx. 9 minutes).

### 5.3 Asymmetric three-point bending test

In this third example, we consider the asymmetric three-point bending test [58, 56, 3]. Here, the fracture grows and we examine the performance of the iteration on the linearization and its influence on the solution. The configuration is displayed in Figure 11. We consider a two dimensional domain with three holes. The boundary conditions are taken from [16]. On  $\partial\Omega_{\text{top}}$ , the upper boundary, we apply time-dependent non-homogeneous Dirichlet conditions in  $y$ -direction in a Gaussian bell curve fashion:

$$u_y = -10 \exp\left(-\frac{(x-10)^2}{100}\right) t \cdot 1\text{mm/s}, \quad x \in [0, 10], \quad t \in [0, T],$$

where  $T > 0$  is the maximum time. Furthermore, we fix the displacement in both directions at  $(1, 0)$  and in  $y$ -direction at  $(19, 0)$ . Otherwise, the boundary conditions are defined to be traction-free (homogeneous Neumann conditions). The material and numerical parameters for this test are provided in Table 7. Two different final configurations are depicted in Figure 12 and Figure 13. As it can be seen there, the crack path from the point, where the fracture exceeds the second hole depends on the mesh. In [56] the authors also observe different crack paths depending on different solution approaches. However, as in [3], we are mainly interested in the simulation results before the fracture grows into the second hole. Thus, we always stop the simulation, once the crack reaches the second hole.

In Figure 16 - Figure 23, we compare the number of active set iterations and the crack energy for two different situations: no ItL and ItE with a tolerance of  $\text{TOL}_{\text{ItL}} = 10^{-3}$  (see Algorithm 3)

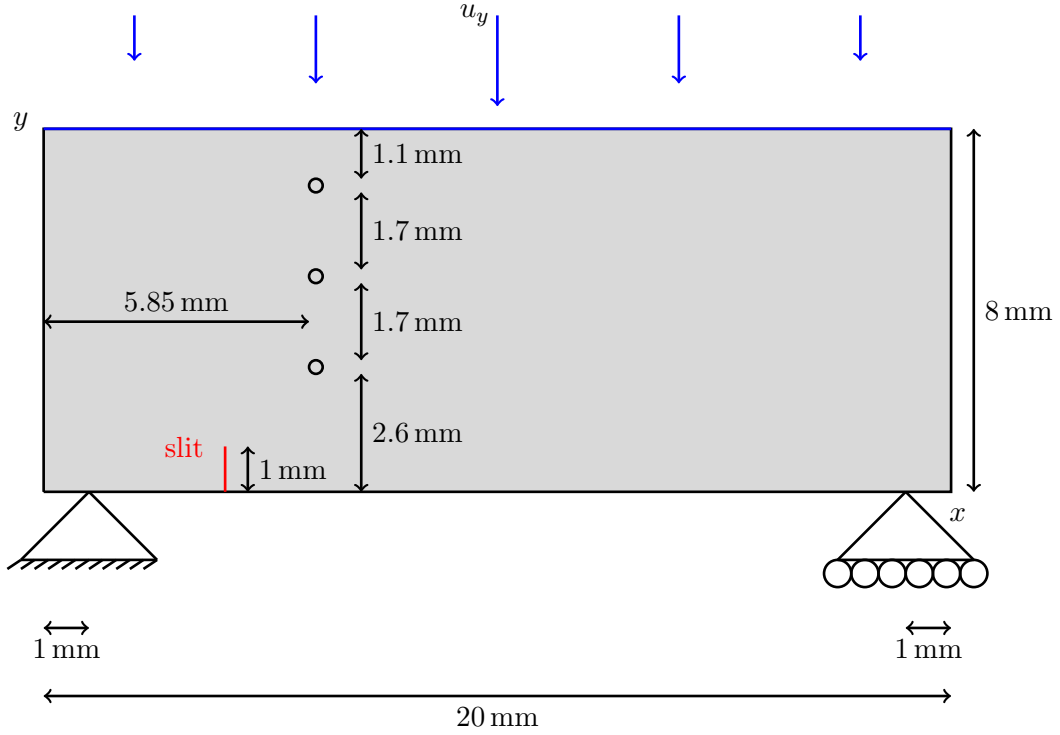


Figure 11: Visualization of the configuration of the asymmetric three-point bending test.

Parameter	Definition	Value
$\Omega$	Domain	$(0, 20) \quad (0, 8)$ (mm)
$h$	Diagonal cell diameter	test-dependent
$G_C$	Material toughness	1.0N/mm
$E$	Young's modulus	1.0kN/mm <sup>2</sup>
$\mu$	Lamé parameter	8.0kN/mm <sup>2</sup>
$\lambda$	Lamé parameter	12.0kN/mm <sup>2</sup>
$\nu$	Poisson's ratio	0.3
$\varepsilon$	Bandwidth of the initial crack	$2h$ (mm)
$\kappa$	Regularization parameter	$10^{-10}h$ (mm)
$k_n$	Time step size	$10^{-4}$ s
	Number of global refinements	2
	Number of local refinements	1, 2, 3, 4
$TOL_N$	Tolerance outer Newton solver	$10^{-7}$
	Tolerance inner linear solver	$\mathbf{k}\tilde{R}(U_h^{n,k})\mathbf{k}_2 10^{-8}$
$TOL_{ItL}$	Tolerance ItL	$10^{-3}$

Table 7: The setting of the material and numerical parameters used for the asymmetric three-point bending test.

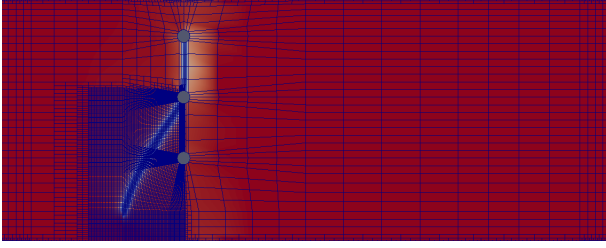


Figure 12: Visualization of the final configuration of the fracture asymmetric three-point bending test with 2 global and 3 local refinements. Red represents the fully intact part of the domain, blue the fully broken part and white stands for the transition zone.

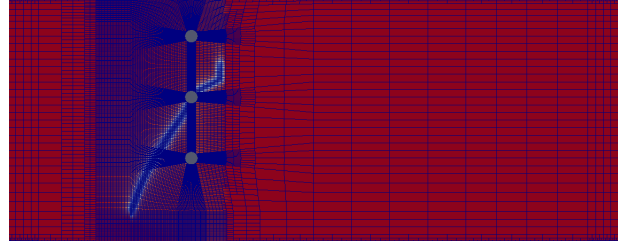


Figure 13: Visualization of the final configuration of the fracture asymmetric three-point bending test with 2 global and 3 local refinements. Red represents the fully intact part of the domain, blue the fully broken part and white stands for the transition zone.

as  $L^2$ -difference. At the highest, around 160 iterations on the linearizations were performed within one incremental step. Usually, within incremental steps without crack development, 2 iterations are sufficient. The crack energy can be computed via

$$E_C = \frac{G_c}{2} \int_{\Omega} \frac{(\varphi - 1)^2}{\varepsilon} d\Omega.$$

We observe that with ItE, the material tears within one incremental step completely (from the tip of the initial fracture into the second hole, see Figure 14 and Figure 15), whereas the crack evolves much slower without ItE. The former is the expected behaviour since the model is designed to represent brittle fractures. Additionally, without ItE, the time of full rupture differs much considering different refinement levels. This indicates that the influence of the mesh on the fracture development is less significant with ItE.

As before we want to give a short comment on the parallel performance for the mesh size  $h = 0.039$ . Moreover, we investigate both without ItE and ItE. Without any iteration on the linearization and on 1 core, the CPU time for one incremental step is 678s (approx. 11.3 minutes), and on 16 cores we observed a CPU time of 59s. With ItE, we have a CPU time of 2207s (approx. 36 minutes) on 1 core and 174s (approx. 2.9 minutes) on 16 cores for one incremental step (with 2 ItE iterations). This demonstrates clearly the balance of accuracy and efficiency whether ItE is used or not.



Figure 14: Visualization of the fracture asymmetric three-point bending test with  $h = 0.019$  after 146 incremental steps with ItE. Red represents the fully intact part of the domain, blue the fully broken part and white stands for the transition zone.



Figure 15: Visualization of the fracture asymmetric three-point bending test with  $h = 0.019$  after 147 incremental steps with ItE. Red represents the fully intact part of the domain, blue the fully broken part and white stands for the transition zone.

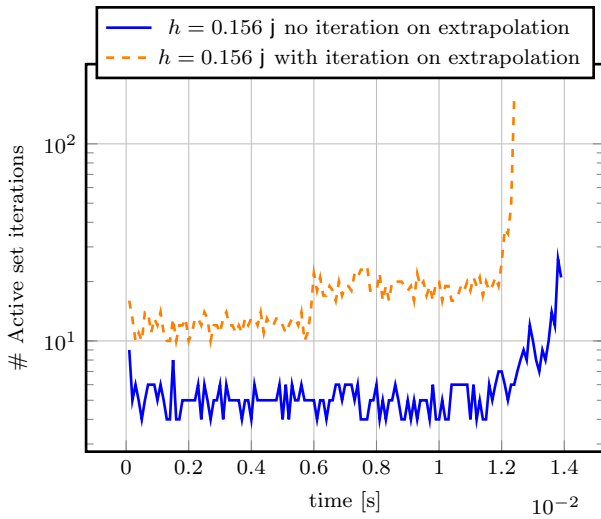


Figure 16: Number of active set iterations ( $y$ -axis) with and without iteration on the extrapolation and  $h = 0.156$  depending on the time ( $x$ -axis) for the asymmetric three-point bending test.

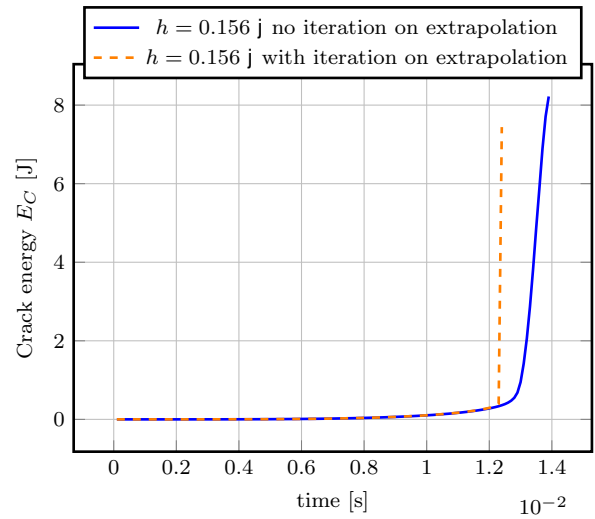


Figure 17: Visualization of the crack energy ( $y$ -axis) with and without iteration on the extrapolation and  $h = 0.156$  depending on the time ( $x$ -axis) for the asymmetric three-point bending test.

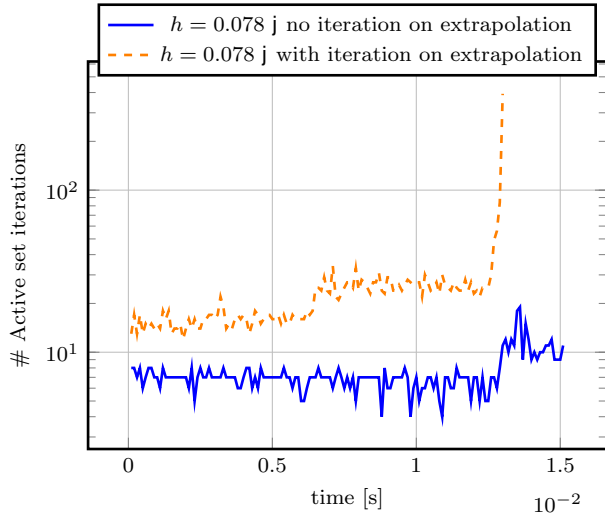


Figure 18: Number of active set iterations ( $y$ -axis) with and without iteration on the extrapolation and  $h = 0.078$  depending on the time ( $x$ -axis) for the asymmetric three-point bending test.

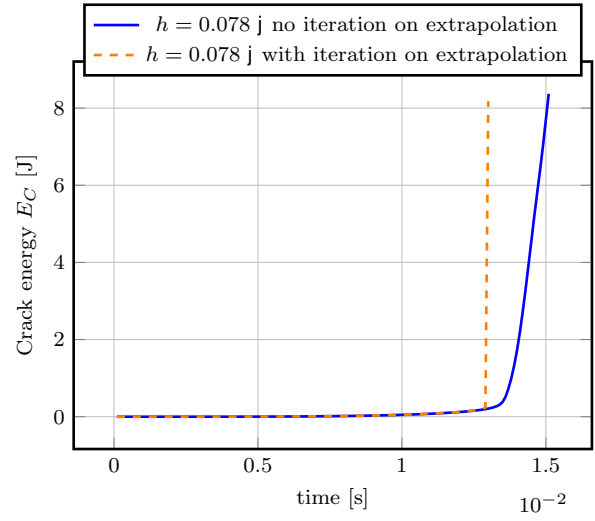


Figure 19: Visualization of the crack energy ( $y$ -axis) with and without iteration on the extrapolation and  $h = 0.078$  depending on the time ( $x$ -axis) for the asymmetric three-point bending test.

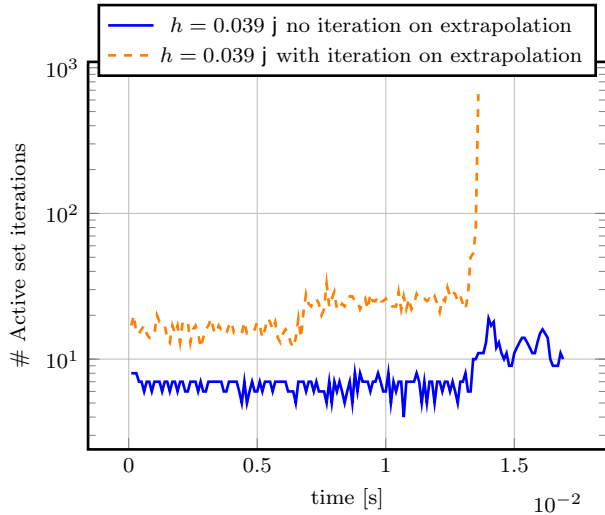


Figure 20: Number of active set iterations ( $y$ -axis) with and without iteration on the extrapolation and  $h = 0.039$  depending on the time ( $x$ -axis) for the asymmetric three-point bending test.

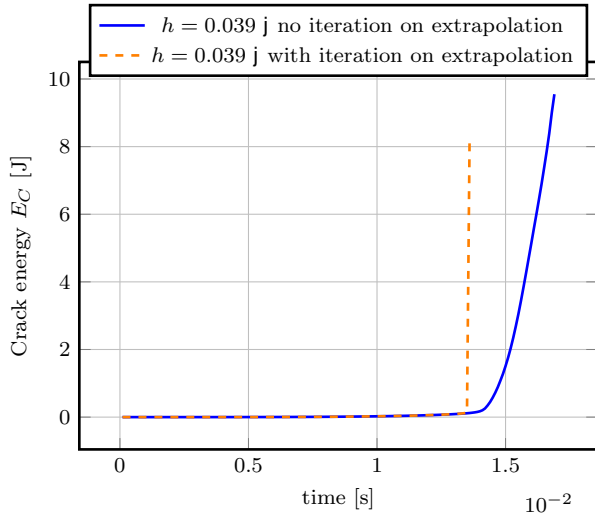


Figure 21: Visualization of the crack energy ( $y$ -axis) with and without iteration on the extrapolation and  $h = 0.039$  depending on the time ( $x$ -axis) for the asymmetric three-point bending test.

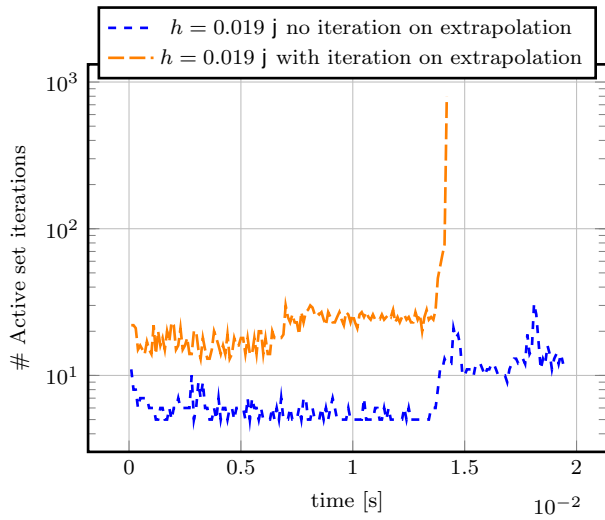


Figure 22: Number of active set iterations ( $y$ -axis) with and without iteration on the extrapolation and  $h = 0.019$  depending on the time ( $x$ -axis) for the asymmetric three-point bending test.

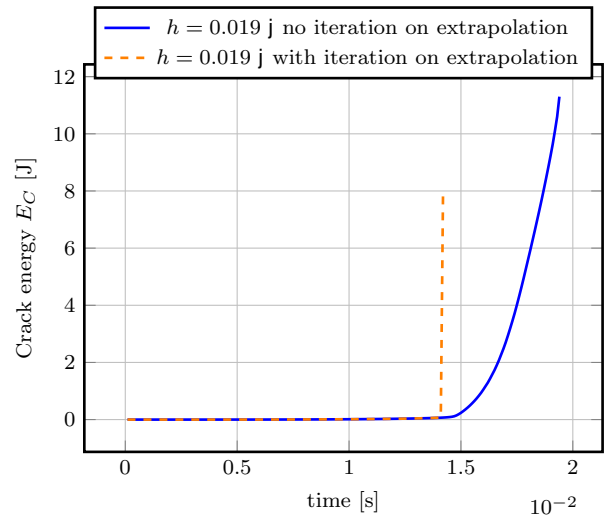


Figure 23: Visualization of the crack energy ( $y$ -axis) with and without iteration on the extrapolation and  $h = 0.019$  depending on the time ( $x$ -axis) for the asymmetric three-point bending test.

#### 5.4 L-shaped panel test

The L-shaped panel test is a well-known test from mechanics, which was originally developed by Winkler [79] to analyze possible crack behaviour of concrete under force experimentally as well as numerically. Further numerical simulations in connection to variational/phase-field solution approaches are performed in [3, 27, 56, 76, 54, 53]. In Figure 24, the geometry  $\Omega$  of the L-shaped panel test is depicted. There exist two configurations of the loading boundary conditions: first monotone loading, and second, a cyclic loading test. In the following, we have the latter in mind.

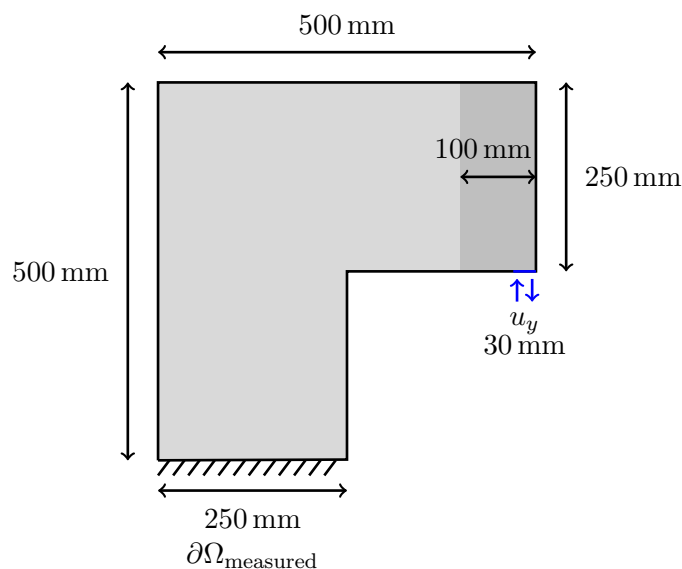


Figure 24: Visualization of the geometry of the L-shaped panel test.



Specifically, we apply a cyclic displacement as non-homogeneous time-dependent Dirichlet conditions [3] at a strip of 30mm length on the right corner of the domain:

$$u_y = t, \quad 0.0\text{s} \leq t \leq 0.3\text{s} \quad (9)$$

$$u_y = 0.6 - t, \quad 0.3\text{s} \leq t \leq 0.8\text{s} \quad (10)$$

$$u_y = t - 1.0, \quad 0.8\text{s} \leq t \leq 2.0\text{s}, \quad (11)$$

where  $t$  represents the simulation time. On the lower boundary  $\partial\Omega_{\text{measure}}$ , we fix the displacement in  $x$ - and  $y$ -direction with homogeneous Dirichlet conditions as  $u_x = u_y = 0$ . On the other boundaries, we apply homogeneous Neumann conditions. As done in [56], in order to avoid the development of nonphysical fractures around the right edge of the specimen, the phase field is constrained with  $\varphi = 1$  for  $x > 400\text{mm}$ . As quantities of interest, we observe the number of Newton iterations and the load on the bottom boundary  $\partial\Omega_{\text{measure}}$ , computed via

$$(F_x, F_y) := \int_{\partial\Omega_{\text{measure}}} \sigma(u_h) \cdot \eta \, ds, \quad (12)$$

where  $\eta$  is the unit normal vector. The parameters for this test are displayed in Table 8.

Parameter	Definition	Value
$\Omega$	Domain	$((0, 0) \quad (250, 500)) \cup ((250, 250) \quad (500, 500))$ (mm)
$h$	Diagonal cell diameter	test-dependent
$G_C$	Material toughness	$8.9 \cdot 10^{-2} \text{N/mm}$
$E$	Young's modulus	$10.677333 \text{kN/mm}^2$
$\mu$	Lamé parameter	$10.95 \text{kN/mm}^2$
$\lambda$	Lamé parameter	$6.16 \text{kN/mm}^2$
$\nu$	Poisson's ratio	0.3
$\varepsilon$	Bandwidth of the initial crack	$2h$ (mm)
$\kappa$	Regularization parameter	$10^{-10} h$ (mm)
$k_n$	Time step size	$10^{-3} \text{s}$
	Number of global refinements	2, 3, 4, 5
	Number of local refinements	0
TOL <sub>N</sub>	Tolerance outer Newton solver	$10^{-7}$
	Tolerance inner linear solver	$\mathbf{k}\tilde{R}(U_h^{n,k})\mathbf{k}_2 10^{-8}$
TOL <sub>ItL</sub>	Tolerance ItL	$10^{-1}$

Table 8: The setting of the material and numerical parameters used for the L-shaped panel test.

A typical final configuration on a globally refined mesh with diagonal element diameter  $h = 1.822$  is displayed in Figure 25. Figure 26-33 visualize the number of active set iterations (as before plus Newton, i.e., combined Newton iterations are given) per incremental step using **Case 2** from Section 3.4.2 and the load displacement curves with no ItL as well as ItE with a tolerance of  $\text{TOL}_{\text{ItL}} = 10^{-1}$  (see Algorithm 3) as  $L^2$ -difference and for four different global refinement levels. On each refinement

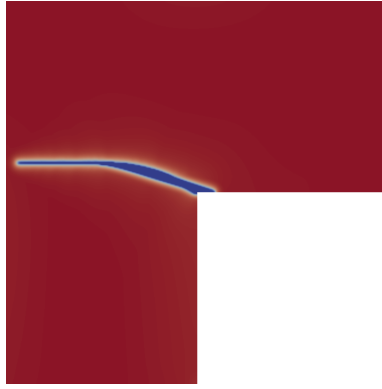


Figure 25: Visualization of the final configuration of the L-shaped panel test with  $h = 1.822$ . Red represents the fully intact part of the domain, blue the fully broken part and white stands for the transition zone.

level, we observe the benefit of ItE as the load decreases faster than with no ItL, i.e. the fracture evolves faster. However, the additional computational cost is also obvious as in the incremental steps of crack evolvement the number of active set iterations is much higher than with no ItL.

For the parallel performance we compare, as in the previous examples, the CPU time for one incremental step on a 5 times globally refined mesh with  $h = 1.82217$  (232323 degrees of freedom). With ItE and on 1 core, the CPU time for one incremental step (and 2 iterations on the extrapolation) is 2094s (approx. 34.9 minutes), whereas on 16 cores it is 154s (approx. 2.6 minutes). With no ItL and on 1 core, 1109s (approx. 18.5 minutes) are needed and 76s (approx. 1.3 minutes) on 16 cores.

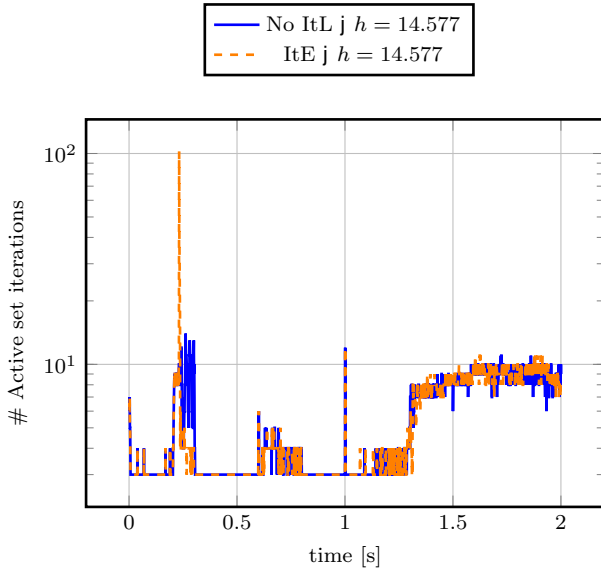


Figure 26: Visualization of the number of active set iterations ( $y$ -axis) with and without iteration on the extrapolation (ItE) and  $h = 14.577$  depending on the time ( $x$ -axis) for the L-shaped panel test.

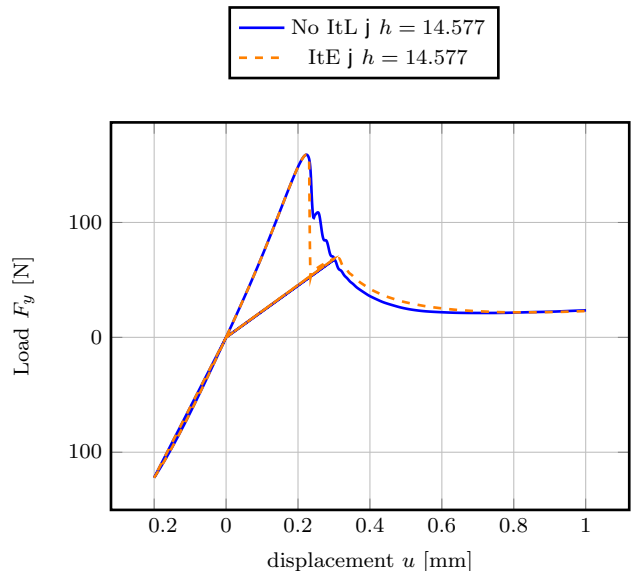


Figure 27: Visualization of the  $y$ -load ( $y$ -axis) with and without iteration on the extrapolation (ItE) and  $h = 14.577$  depending on the displacement ( $x$ -axis) for the L-shaped panel test.

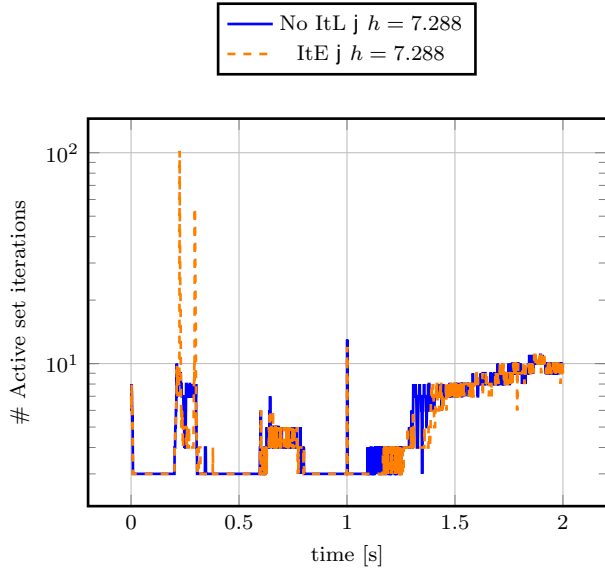


Figure 28: Visualization of the number of active set iterations ( $y$ -axis) with and without iteration on the extrapolation (ItE) and  $h = 7.288$  depending on the time ( $x$ -axis) for the L-shaped panel test.

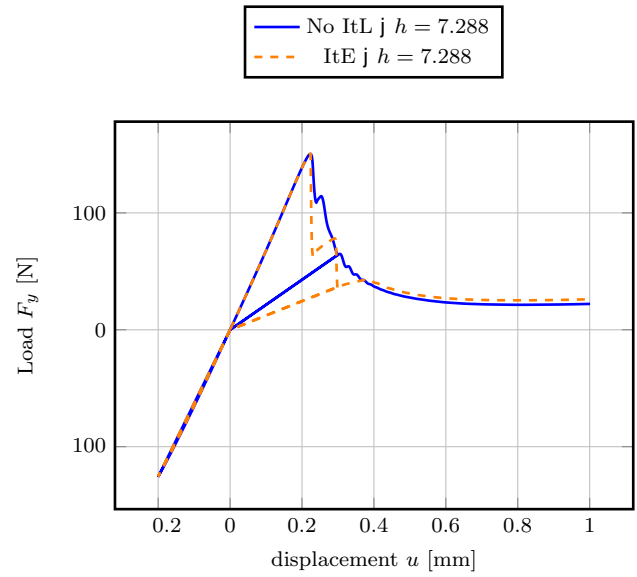


Figure 29: Visualization of the  $y$ -load ( $y$ -axis) with and without iteration on the extrapolation (ItE) and  $h = 7.288$  depending on the displacement ( $x$ -axis) for the L-shaped panel test.

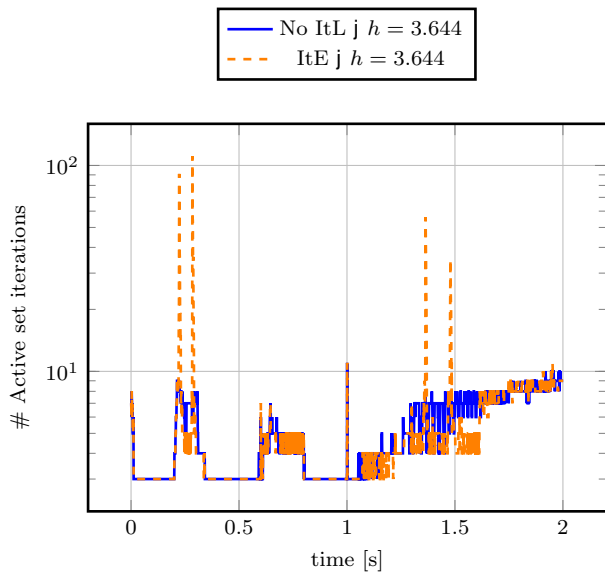


Figure 30: Visualization of the number of active set iterations ( $y$ -axis) with and without iteration on the extrapolation (ItE) and  $h = 3.644$  depending on the time ( $x$ -axis) for the L-shaped panel test.

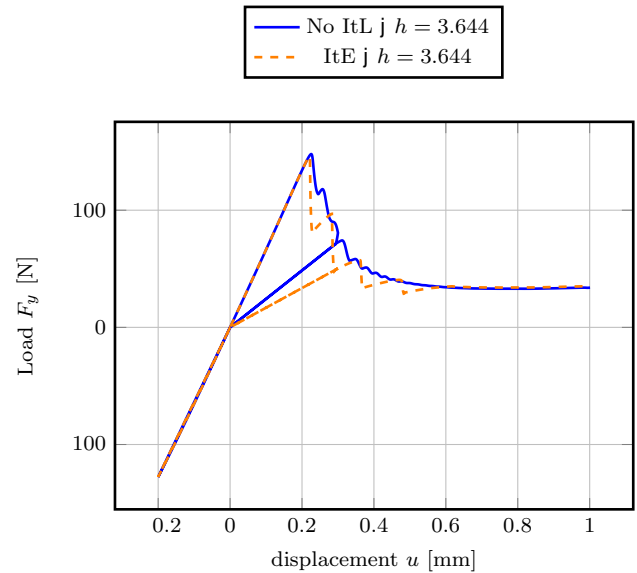


Figure 31: Visualization of the  $y$ -load ( $y$ -axis) with and without iteration on the extrapolation (ItE) and  $h = 3.644$  depending on the displacement ( $x$ -axis) for the L-shaped panel test.

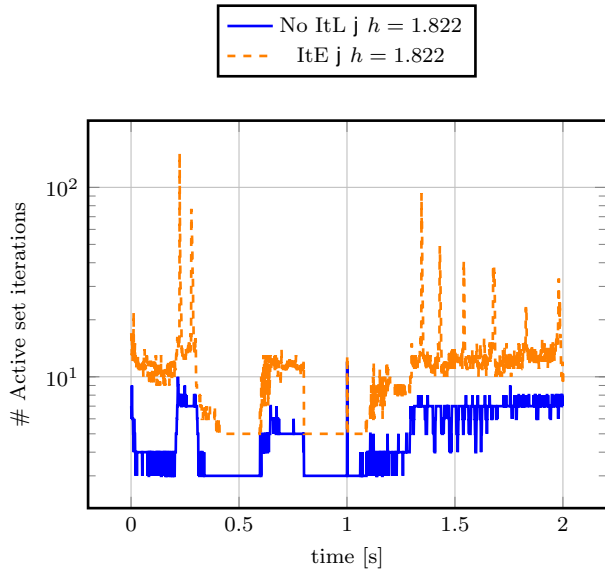


Figure 32: Visualization of the number of active set iterations ( $y$ -axis) with and without iteration on the extrapolation (ItE) and  $h = 1.822$  depending on the time ( $x$ -axis) for the L-shaped panel test.

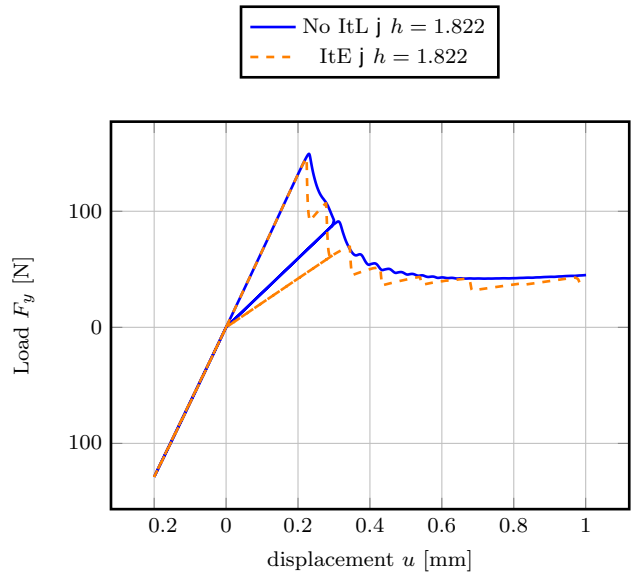


Figure 33: Visualization of the  $y$ -load ( $y$ -axis) with and without iteration on the extrapolation (ItE) and  $h = 1.822$  depending on the displacement ( $x$ -axis) for the L-shaped panel test.

## 5.5 Single edge notched shear test

In the last example, we consider the single-edge notched shear (SENS), see for instance [58, 57]. A visualization and explanation is displayed in Figure 34. The domain  $\Omega$  is a two dimensional square

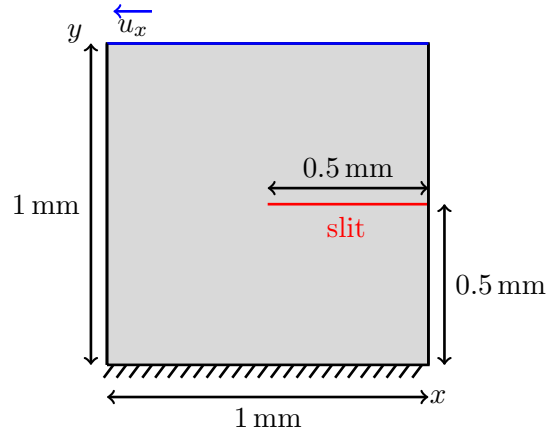


Figure 34: Visualization of the geometry of the single edge notched shear test.

of 1 mm length with a given crack (called geometrical slit) on the right side at 5 mm tending to the midpoint of the square. On the bottom boundary, the square is fixed, and on the top boundary, a given displacement in the  $x$ -direction pulls to the left. The boundary conditions can be found for instance in [77]: On the left and right sides, the boundaries are defined to be traction-free (homogeneous Neumann conditions). The bottom boundary is fixed via  $u_x = u_y = 0$  mm. On the top boundary, it holds  $u_y = 0$  mm and in the  $x$ -direction we determine a time-dependent non-homogeneous Dirichlet condition:  $u_x = t_n \cdot 1$  mm/s, where  $t_n$  is the  $n$ -th incremental step. The end time  $T$  is the incremental step once the specimen is broken. The parameters for this test are given in Table 9. A standard final configuration of this test example is depicted in Figure 35.

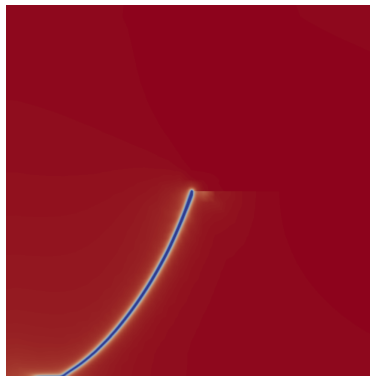


Figure 35: Visualization of the fracture for the SENS test with  $h = 0.0027$  in the final configuration after 135 incremental steps with ItE. Red represents the fully intact part of the domain, blue the fully broken part and white stands for the transition zone.

As a quantity of interest, we evaluate the load functions on the top boundary  $\partial\Omega_{\text{top}}$  computed via

$$(F_x, F_y) := \int_{\partial\Omega_{\text{top}}} \sigma(u_h) \cdot \eta \, ds, \quad (13)$$

with the stress tensor  $\sigma(u_h)$  depending on the discrete solution variable  $u_h$  and the outer normal vector  $\eta$ . Within the single-edge notched shear test, we are interested in the evaluation of  $F_x$ .

Parameter	Definition	Value
$\Omega$	Domain	$(0, 1)^2$ (mm)
$h$	Diagonal cell diameter	test-dependent
$G_C$	Material toughness	2.7N/mm
$\mu$	Lamé parameter	80.77kN/mm <sup>2</sup>
$\lambda$	Lamé parameter	121.15kN/mm <sup>2</sup>
$\nu$	Poisson's ratio	0.2
$\varepsilon$	Bandwidth of the initial crack	$2h$ (mm)
$\kappa$	Regularization parameter	$10^{-10}h$ (mm)
$k_n$	Time step size	$10^{-4}$ s
	Number of global refinements	2
	Number of local refinements	1, 2, 3, 4
TOL <sub>N</sub>	Tolerance outer Newton solver	$10^{-7}$
	Tolerance inner linear solver	$\mathbf{k}\tilde{R}(U_h^{n,k})\mathbf{k}_2 10^{-8}$
TOL <sub>ItL</sub>	Tolerance ItL	$10^{-1}$

Table 9: The setting of the material and numerical parameters used for the SENS-test.

Similar to the asymmetric three-point bending test, we want to investigate the advantages and possible drawbacks of an iteration into the monolithic limit using ItL. As before, we compare the crack energy and the corresponding Newton active set iterations for two different approaches: In one situation, we only compute the linearization and solve the system with the Newton method once per incremental step. In the second situation, we iterate, as described before, until the  $L^2$ -norm of the difference between two consecutive solutions is small enough up to a given tolerance. Since we observe non-physical behaviour (Figure 41) when using ItE<sup>1</sup>, we also consider ItOTS as a third approach. We compare the total number of Newton active set iterations per incremental step and the  $x$ -load. For both ItE and ItOTS, we choose a tolerance of TOL<sub>ItL</sub> =  $10^{-1}$  (see Algorithm 3) as  $L^2$ -difference. The results are visualized in Figure 39 - Figure 45. We also examine varying ItL tolerances and Newton tolerances, but found that both do not influence the solution. For ItL, a smaller tolerance only leads to a larger computation time since more iterations are necessary, but the solution does not differ significantly. For the Newton tolerance, the residual norm converges faster than the active set, such that the final residual norm is of magnitude around  $10^{-10}$  no matter which tolerance is handed over.

<sup>1</sup>We are aware of [3] who found that the Miehe et al. splitting [58] is not a good choice here. But this does not alter our solver investigations we have primarily in mind.

We observe that on all refinement levels that fracture evolves much faster with ItE than with ItOTS or no ItL. This confirms findings made in [76][Fig. 3] in which the extrapolated scheme (no ItL) is compared to a fully monolithic scheme. However with ItE, for  $h = 0.022, 0.011, 0.0055$ , the load shows unphysical behaviour: at a certain point, the fracture stops growing and the load increases again until it reaches a local peak. Then, the crack continues to propagate until the material is fully ruptured. From a physical perspective, we expect the fracture to fully evolve within a few incremental steps once it starts to evolve. This behaviour is less significant, when using ItOTS or no ItL. For the number of Newton active set iterations, no ItL needs less iterations than ItE and ItOTS. This is clear since without ItL, in each incremental step the system is only solved once per predictor-corrector refinement step, whereas with ItE and ItOTS, the system may be solved many times per predictor-corrector refinement step. Overall, ItE needs less iterations than ItOTS, but the peaks are of similar magnitude. The peaks occur in the incremental steps, where the crack evolves, with around 40 iterations on the linearizations. In incremental steps without crack evolvment, around 2 iterations on the linearization suffice to fall below  $10^{-1}$ .

Specifically on finer meshes, both ItL approaches yield a faster growing crack, that is closer to the true physics of the governing model (see again [76, 77]), but, of course, at the cost of performance. Since the same incremental step is solved several times due to the ItL (and also the adaptive mesh refinement), the number of Newton active set iterations becomes very high for critical incremental steps.

Lastly, we again want to show the parallel performance by comparing the CPU time (the amount of time at least 1 processor works) of one incremental step with no ItL on 1 core and on 16 cores. On 1 core, the CPU time is 647s (approx. 10.6 minutes) and on 16 cores, it is 39s.

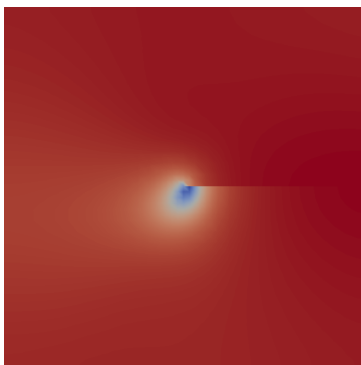


Figure 36: Visualization of the fracture for the SENS test with  $h = 0.022$  after 100 incremental steps with no ItL. Red represents the fully intact part of the domain, blue the fully broken part and white stands for the transition zone.

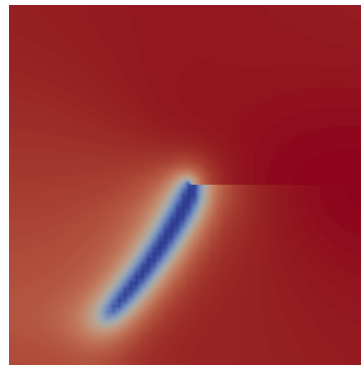


Figure 37: Visualization of the fracture for the SENS test with  $h = 0.022$  after 100 incremental steps with ItE. Red represents the fully intact part of the domain, blue the fully broken part and white stands for the transition zone.

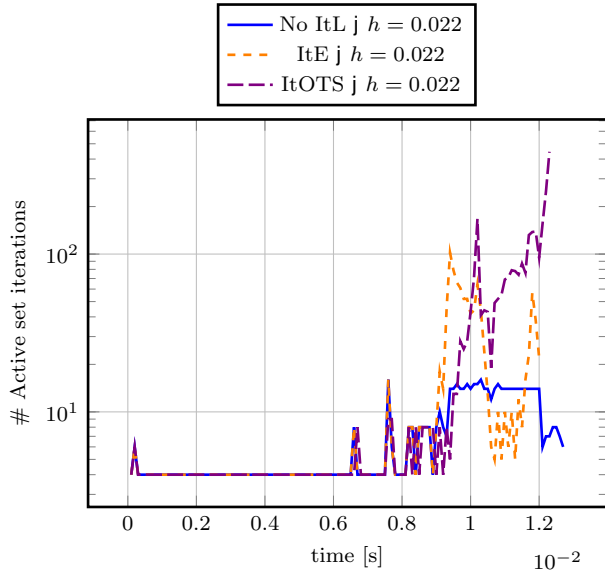


Figure 38: Visualization of the number of active set iterations ( $y$ -axis) with and without iteration on the linearization (ItE and ItOTS) and  $h = 0.022$  depending on the time ( $x$ -axis) for the SENS test.

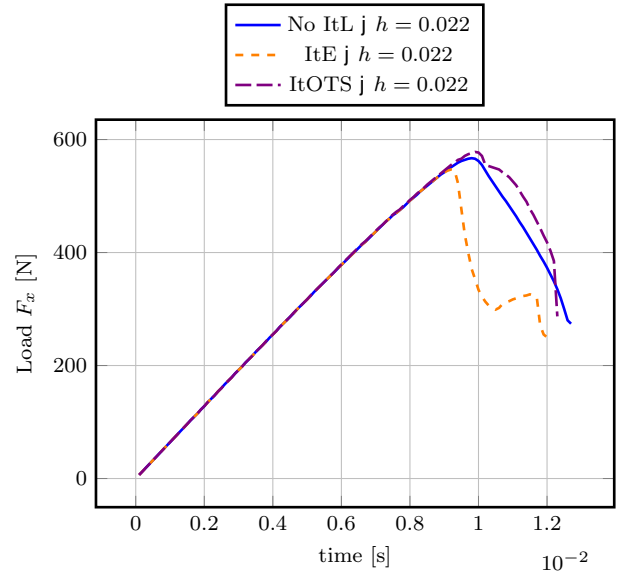


Figure 39: Visualization of the  $x$ -load displacement ( $y$ -axis) with and without iteration on the linearization (ItE and ItOTS) and  $h = 0.022$  depending on the time ( $x$ -axis) for the SENS test.

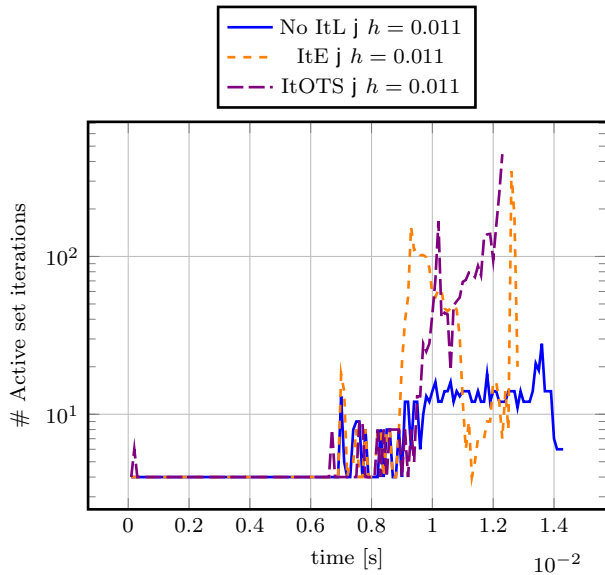


Figure 40: Visualization of the number of active set iterations ( $y$ -axis) with and without iteration on the linearization (ItE and ItOTS) and  $h = 0.011$  depending on the time ( $x$ -axis) for the SENS test.

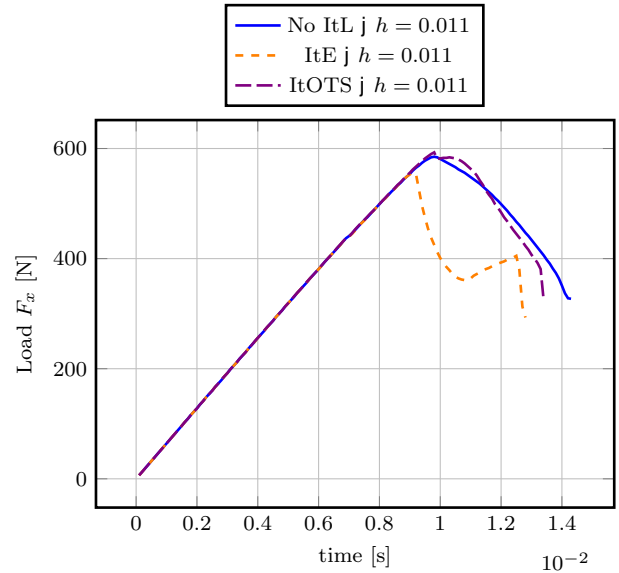


Figure 41: Visualization of the  $x$ -load displacement ( $y$ -axis) with and without iteration on the linearization (ItE and ItOTS) and  $h = 0.011$  depending on the time ( $x$ -axis) for the SENS test.



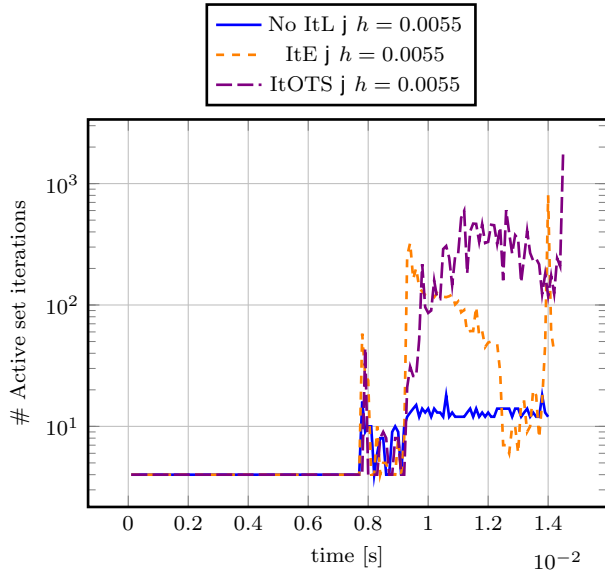


Figure 42: Visualization of the number of active set iterations ( $y$ -axis) with and without iteration on the linearization (ItE and ItOTS) and  $h = 0.0055$  depending on the time ( $x$ -axis) for the SENS test.

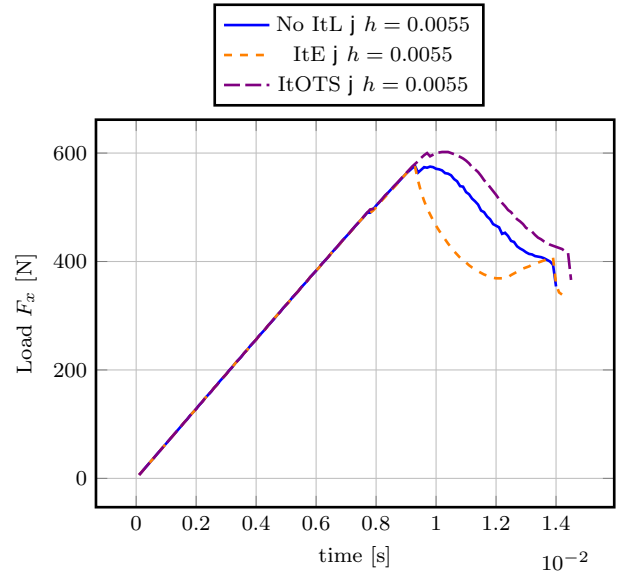


Figure 43: Visualization of the  $x$ -load displacement ( $y$ -axis) with and without iteration on the linearization (ItE and ItOTS) and  $h = 0.0055$  depending on the time ( $x$ -axis) for the SENS test.

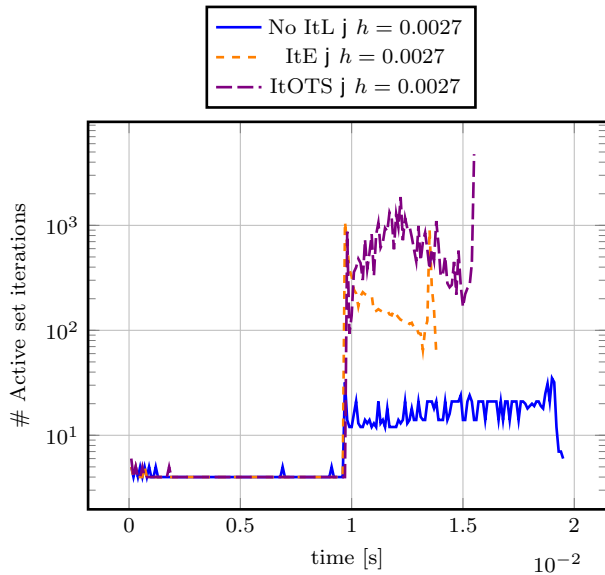


Figure 44: Visualization of the number of active set iterations ( $y$ -axis) with and without iteration on the linearization (ItE and ItOTS) and  $h = 0.0027$  depending on the time ( $x$ -axis) for the SENS test.

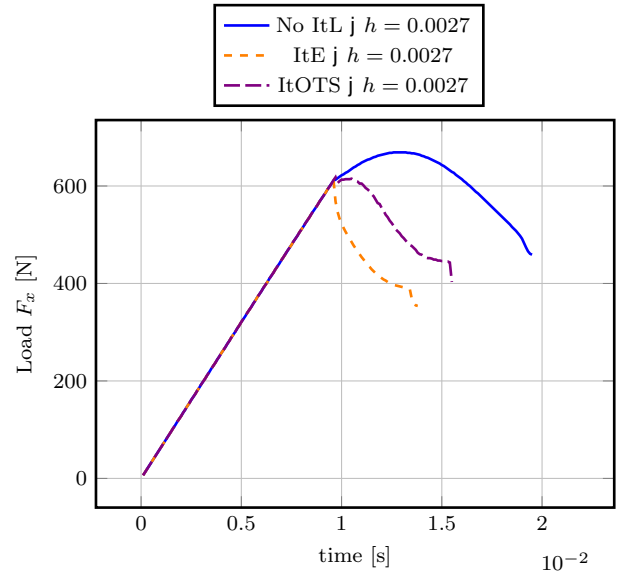


Figure 45: Visualization of the  $x$ -load displacement ( $y$ -axis) with and without iteration on the linearization (ItE and ItOTS) and  $h = 0.0027$  depending on the time ( $x$ -axis) for the SENS test.

## 6 Conclusion

In this work, we investigated and improved the primal-dual active set phase-field fracture formulation proposed in [32]. From the three major advancements is one of theoretical nature and two are numerically motivated. On the theoretical side we worked out details of deriving the active set formulation from the governing complementarity system. In numerics, we examined the active set constant  $c$  and proposed four different test cases to be compared. Thirdly, we studied an iteration on the linearization procedure of the phase-field variable in the displacement equation. Concerning the derivations established in Section 2, we started from the coupled variational inequality system (CVIS) and derived the complementarity formulation in weak form. Then, this was linked to the corresponding strong form conditions, which are the starting point for the active set algorithm. In Section 3, we investigated theoretically the role of the active set constant  $c$  in the solution algorithm and found a new setting, which avoids the wrong classification of degrees of freedom. This increases the convergence speed of the Newton active set method on fine meshes and thus yields better performances. In Section 4, besides studying the iteration on the linearization, we formulated a final new algorithm. For both linearization approaches, ItL resolves the time-lagging issue, that is due to the resulting discretization error. In Section 5, we performed five numerical tests including two- and three-dimensional settings, as well as stationary crack that only vary in their width, and propagating fractures. In the SENS test (Section 5.5), ItE performs better than ItOTS in terms of fracture evolution speed, but ItE shows some non-physical behaviour due to the iterations on the extrapolation. In terms of accuracy, both approaches yield findings that are closer to the expected physics, as it can be compared with our prior work when using a fully monolithic model. Our overall conclusion of both modifications, namely active set constant and the ItL schemes, is that one has to make a choice between accuracy and efficiency. This is not surprising at all, but highlighted in this work for our primal-dual phase-field fracture framework.

## Acknowledgements

All authors thank Viktor Kossin (Université Paris-Saclay) for fruitful discussions on the iteration on the extrapolation part and Johannes Lankeit (Leibniz University Hannover) for giving valuable advice and comments on solution spaces in connection with equivalence proofs within this work. Moreover, the authors thank Sebastian Bohlmann for the Scientific Computing environment at IfAM. The present work has been partially carried out within the DFG Collaborative Research Center (CRC) 1463 “Integrated design and operation methodology for offshore megastructures”, which is funded by the Deutsche Forschungsgemeinschaft (DFG, German Research Foundation) - Project-ID 434502799, SFB 1463. Moreover, the authors thank the (anonymous) reviewers for their questions that helped to improve the manuscript.

## References

- [1] F. Aldakheel, B. Hudobivnik, M. Soleimani, H. Wessels, C. Weissenfels, and M. Marino, editors. *Current Trends and Open Problems in Computational Mechanics*. Springer Cham, 2022.
- [2] F. Aldakheel, N. Noii, T. Wick, O. Allix, and P. Wriggers. Multilevel global–local techniques for adaptive ductile phase-field fracture. *Comput. Methods Appl. Mech. Engrg.*, 387:114175, 2021.
- [3] M. Ambati, T. Gerasimov, and L. De Lorenzis. A review on phase-field models of brittle fracture and a new fast hybrid formulation. *Comput. Mech.*, 55(2):383–405, 2015.
- [4] L. Ambrosio and V. M. Tortorelli. Approximation of functional depending on jumps by elliptic functional via t-convergence. *Comm. Pure Appl. Math*, 43(8):999–1036, 1990.
- [5] L. Ambrosio and V. M. Tortorelli. On the approximation of free discontinuity problems. *Boll. Un. Mat. Ital. B (7)*, 6(1):105–123, 1992.
- [6] D. Arndt, W. Bangerth, D. Davydov, T. Heister, L. Heltai, M. Kronbichler, M. Maier, J.-P. Pelteret, B. Turcksin, and D. Wells. The deal.II finite element library: Design, features, and insights. *Comput. Math. Appl.*, 81:407–422, 2021.
- [7] D. Arndt, W. Bangerth, M. Feder, M. Fehling, R. Gassmüller, T. Heister, L. Heltai, M. Kronbichler, M. Maier, P. Munch, J.-P. Pelteret, S. Stiecko, B. Turcksin, and D. Wells. The deal.II library, version 9.4. *J. Numer. Math.*, 30(3):231–246, 2022.
- [8] M. Bergounioux, M. Haddou, M. Hintermüller, and K. Kunisch. A comparison of a Moreau-Yosida-based active set strategy and interior point methods for constrained optimal control problems. *SIAM J. Optim.*, 11(2):495–521, 2000.
- [9] M. Bergounioux, K. Ito, and K. Kunisch. Primal-dual strategy for constrained optimal control problems. *SIAM J. Control Optim.*, 37(4):1176–1194, 1999.
- [10] R. Bharali, S. Goswami, C. Anitescu, and T. Rabczuk. A robust monolithic solver for phase-field fracture integrated with fracture energy based arc-length method and under-relaxation. *Comput. Methods Appl. Mech. Engrg.*, 394:114927, 2022.
- [11] B. Bourdin. Numerical implementation of the variational formulation for quasi-static brittle fracture. *Interfaces Free Bound.*, 9:411–430, 2007.
- [12] B. Bourdin, G. Francfort, and J.-J. Marigo. The variational approach to fracture. *J. Elasticity*, 91(1–3):1–148, 2008.
- [13] B. Bourdin and G. A. Francfort. Past and present of variational fracture. *SIAM News*, 52(9), 2019.

- [14] B. Bourdin, G. A. Francfort, and J.-J. Marigo. Numerical experiments in revisited brittle fracture. *J. Mech. Phys. Solids*, 48(4):797–826, 2000.
- [15] A. Braides. *Approximation of free-discontinuity problems*. Springer Berlin Heidelberg, 1998.
- [16] M. K. Brun, T. Wick, I. Berre, J. M. Nordbotten, and F. A. Radu. An iterative staggered scheme for phase field brittle fracture propagation with stabilizing parameters. *Comput. Methods Appl. Mech. Engrg.*, 361:112752, 2020.
- [17] S. Burke, C. Ortner, and E. Süli. An adaptive finite element approximation of a variational model of brittle fracture. *SIAM J. Numer. Anal.*, 48(3):980–1012, 2010.
- [18] S. Burke, C. Ortner, and E. Süli. An adaptive finite element approximation of a generalized Ambrosio-Tortorelli functional. *Math. Models Methods Appl. Sci.*, 23(9):1663–1697, 2013.
- [19] P. G. Ciarlet. *The finite element method for elliptic problems*, volume 40 of *Classics Appl. Math.* SIAM, Philadelphia, PA, 2002. Reprint of the 1978 original [North-Holland, Amsterdam].
- [20] F. E. Curtis, Z. Han, and D. P. Robinson. A globally convergent primal-dual active-set framework for large-scale convex quadratic optimization. *Comput. Optim. Appl.*, 60(2):311–341, Mar 2015.
- [21] P. Diehl, R. Lipton, T. Wick, and M. Tyagi. A comparative review of peridynamics and phase-field models for engineering fracture mechanics. *Computational Mechanics*, 69:1259–1293, 2022.
- [22] C. Engwer and L. Schumacher. A phase field approach to pressurized fractures using discontinuous galerkin methods. *Math. Comput. Simul.*, 137:266–285, 2016.
- [23] L. C. Evans. *Partial differential equations*. American Mathematical Society, 2010.
- [24] P. E. Farrell and C. Maurini. Linear and nonlinear solvers for variational phase-field models of brittle fracture. *Int. J. Numer. Meth. Engrg.*, 109:648–667, 2017.
- [25] G. Francfort and J.-J. Marigo. Revisiting brittle fracture as an energy minimization problem. *J. Mech. Phys. Solids*, 46(8):1319–1342, 1998.
- [26] R. Geelen, J. Plews, M. Tupek, and J. Dolbow. An extended/generalized phase-field finite element method for crack growth with global-local enrichment. *Int. J. Numer. Meth. Engrg.*, 121(11):2534–2557, 2020.
- [27] T. Gerasimov and L. D. Lorenzis. A line search assisted monolithic approach for phase-field computing of brittle fracture. *Comput. Methods Appl. Mech. Engrg.*, 312:276 – 303, 2016.
- [28] T. Gerasimov, N. Nohi, O. Allix, and L. De Lorenzis. A non-intrusive global/local approach applied to phase-field modeling of brittle fracture. *Adv. Model. and Simul. in Eng. Sci.*, 5(1):14, May 2018.

- [29] S. Goswami, C. Anitescu, S. Chakraborty, and T. Rabczuk. Transfer learning enhanced physics informed neural network for phase-field modeling of fracture. *Theor. Appl. Fract. Mech.*, 106:102447, 2020.
- [30] S. Goswami, M. Yin, Y. Yu, and G. E. Karniadakis. A physics-informed variational deep-net for predicting crack path in quasi-brittle materials. *Comput. Methods Appl. Mech. Engrg.*, 391:114587, 2022.
- [31] C. Gräser, D. Kienle, and O. Sander. Truncated nonsmooth newton multigrid for phase-field brittle-fracture problems, 2020, <https://arxiv.org/abs/2007.12290>.
- [32] T. Heister, M. F. Wheeler, and T. Wick. A primal-dual active set method and predictor-corrector mesh adaptivity for computing fracture propagation using a phase-field approach. *Comput. Methods Appl. Mech. Engrg.*, 290:466–495, 2015.
- [33] T. Heister and T. Wick. Parallel solution, adaptivity, computational convergence, and open-source code of 2d and 3d pressurized phase-field fracture problems. *PAMM*, 18(1):e201800353, 2018.
- [34] T. Heister and T. Wick. pfm-cracks: A parallel-adaptive framework for phase-field fracture propagation. *Software Impacts*, 6:100045, 2020.
- [35] M. A. Heroux, R. A. Bartlett, V. E. Howle, R. J. Hoekstra, J. J. Hu, T. G. Kolda, R. B. Lehoucq, K. R. Long, R. P. Pawlowski, E. T. Phipps, A. G. Salinger, H. K. Thornquist, R. S. Tuminaro, J. M. Willenbring, A. Williams, and K. S. Stanley. An overview of the trilinos project. *ACM Trans. Math. Softw.*, 31(3):397–423, 2005.
- [36] M. Hintermüller, K. Ito, and K. Kunisch. The primal-dual active set strategy as a semismooth Newton method. *SIAM J. Optim.*, 13(3):865–888 (2003), 2002.
- [37] S. Hübner and B. Wohlmuth. A primal–dual active set strategy for non-linear multibody contact problems. *Comput. Methods Appl. Mech. Engrg.*, 194(27):3147–3166, 2005.
- [38] K. Ito and K. Kunisch. Augmented Lagrangian methods for nonsmooth, convex optimization in Hilbert spaces. *Nonlinear Anal.*, 41(5-6, Ser. A: Theory Methods):591–616, 2000.
- [39] K. Ito and K. Kunisch. Optimal control of elliptic variational inequalities. *Appl. Math. Optim.*, 41(3):343–364, 2000.
- [40] D. Jodlbauer, U. Langer, and T. Wick. Matrix-free multigrid solvers for phase-field fracture problems. *Comput. Methods Appl. Mech. Engrg.*, 372:113431, 2020.

- [41] T. Kärkkäinen, K. Kunisch, and P. Tarvainen. Augmented Lagrangian active set methods for obstacle problems. *J. Optim. Theory Appl.*, 119(3):499–533, 2003.
- [42] N. Kikuchi and J. T. Oden. *Contact problems in elasticity: a study of variational inequalities and finite element methods*, volume 8 of *Stud. Appl. Math.* SIAM, Philadelphia, PA, 1988.
- [43] L. Kolditz and K. Mang. On the relation of gamma-convergence parameters for pressure-driven quasi-static phase-field fracture. *Ex. Count.*, 2:100047, 2022.
- [44] A. Kopanicakova and R. Krause. A recursive multilevel trust region method with application to fully monolithic phase-field models of brittle fracture. *Comput. Methods Appl. Mech. Engrg.*, 360:112720, 2020.
- [45] A. Kopaničáková, H. Kothari, and R. Krause. Nonlinear field-split preconditioners for solving monolithic phase-field models of brittle fracture. *Comput. Methods Appl. Mech. Engrg.*, 403:115733, 2023.
- [46] P. K. Kristensen and E. Martínez-Pañeda. Phase field fracture modelling using quasi-newton methods and a new adaptive step scheme. *Theor. Appl. Fract. Mech.*, 107:102446, 2020.
- [47] C. Kuhn and R. Müller. A continuum phase field model for fracture. *Engrg. Fract. Mech.*, 77(18):3625 – 3634, 2010. Computational Mechanics in Fracture and Damage: A Special Issue in Honor of Prof. Gross.
- [48] O. Lampron. *Phase-field modeling of fracture in additively manufactured thermoplastic parts*. PhD thesis, Université de Montréal, 2023.
- [49] O. Lampron, D. Therriault, and M. Lévesque. An efficient and robust monolithic approach to phase-field quasi-static brittle fracture using a modified newton method. *Comput. Methods Appl. Mech. Engrg.*, 386:114091, 2021.
- [50] G. Liu, Q. Li, M. A. Msekh, and Z. Zuo. Abaqus implementation of monolithic and staggered schemes for quasi-static and dynamic fracture phase-field model. *Computational Materials Science*, 121:35–47, 2016.
- [51] Z. Liu, J. Reinoso, and M. Paggi. Phase field modeling of brittle fracture in large-deformation solid shells with the efficient quasi-newton solution and global–local approach. *Comput. Methods Appl. Mech. Engrg.*, 399:115410, 2022.
- [52] C. Luo. Fast staggered schemes for the phase-field model of brittle fracture based on the fixed-stress concept. *Comput. Methods Appl. Mech. Engrg.*, 404:115787, 2023.

- [53] K. Mang. *Phase-field fracture modeling, numerical solution, and simulations for compressible and incompressible solids*. PhD thesis, Leibniz Universität Hannover, 2022.
- [54] K. Mang, M. Walloth, T. Wick, and W. Wollner. Adaptive numerical simulation of a phase-field fracture model in mixed form tested on an l-shaped specimen with high poisson ratios. In F. J. Vermolen and C. Vuik, editors, *Numerical Mathematics and Advanced Applications ENUMATH 2019*, pages 1185–1193, Cham, 2021. Springer International Publishing.
- [55] S. May, J. Vignollet, and R. de Borst. A new arc-length control method based on the rates of the internal and the dissipated energy. *Engineering Computations*, 33(1):100–115, 2016.
- [56] A. Mesgarnejad, B. Bourdin, and M. Khonsari. Validation simulations for the variational approach to fracture. *Comput. Methods Appl. Mech. Engrg.*, 290:420 – 437, 2015.
- [57] C. Miehe, M. Hofacker, and F. Welschinger. A phase field model for rate-independent crack propagation: Robust algorithmic implementation based on operator splits. *Comput. Methods Appl. Mech. Engrg.*, 199:2765–2778, 2010.
- [58] C. Miehe, F. Welschinger, and M. Hofacker. Thermodynamically consistent phase-field models of fracture: variational principles and multi-field FE implementations. *Int. J. Numer. Meth. Engng.*, 83:1273–1311, 2010.
- [59] A. Mikelić, M. Wheeler, and T. Wick. A phase-field approach to the fluid filled fracture surrounded by a poroelastic medium. ICES Report 13-15, Jun 2013.
- [60] A. Mikelić, M. F. Wheeler, and T. Wick. A quasi-static phase-field approach to pressurized fractures. *Nonlinearity*, 28(5):1371–1399, 2015.
- [61] A. Mikelić, M. F. Wheeler, and T. Wick. Phase-field modeling through iterative splitting of hydraulic fractures in a poroelastic medium. *GEM - International Journal on Geomathematics*, 10(1), Jan 2019.
- [62] Y. Navidtehrani, C. Betegon, and E. Martinez-Paneda. A unified abaqus implementation of the phase field fracture method using only a user material subroutine. *Materials*, 14(8), 2021.
- [63] Y. Navidtehrani, C. Betegón, and E. Martínez-Pañeda. A simple and robust abaqus implementation of the phase field fracture method. *Appl. Engng. Sci.*, 6:100050, 2021.
- [64] N. Noii, F. Aldakheel, T. Wick, and P. Wriggers. An adaptive global-local approach for phase-field modeling of anisotropic brittle fracture. *Comput. Methods Appl. Mech. Engrg.*, 361:112744, 2020.

- [65] A. Popp, M. W. Gee, and W. A. Wall. A finite deformation mortar contact formulation using a primal–dual active set strategy. *Int. J. Numer. Meth. Engng.*, 79(11):1354–1391, 2009.
- [66] Y. Saad and M. H. Schultz. Gmres: A generalized minimal residual algorithm for solving non-symmetric linear systems. *SIAM J. Sci. Stat. Comput.*, 7(3):856–869, 1986.
- [67] J. Schröder, T. Wick, S. Reese, and et al. A selection of benchmark problems in solid mechanics and applied mathematics. *Arch. Comput. Methods Eng.*, 28(2):713–751, 2021.
- [68] B. Schröder and D. Kuhl. A semi-smooth Newton method for dynamic multifield plasticity. *PAMM*, 16(1):767–768, 2016.
- [69] N. Singh, C. Verhoosel, R. de Borst, and E. van Brummelen. A fracture-controlled path-following technique for phase-field modeling of brittle fracture. *Finite Elem. Anal. Des.*, 113:14–29, 2016.
- [70] I. N. Sneddon. The distribution of stress in the neighbourhood of a crack in an elastic solid. *Proc. R. Soc. Lond. A*, 187(1009):229–260, 1946.
- [71] I. N. Sneddon and M. Lowengrub. *Crack problems in the classical theory of elasticity*. SIAM Ser. Appl. Meth. John Wiley and Sons, Philadelphia, 1969.
- [72] L. Sommer. *An unfitted discontinuous Galerkin scheme for a phase-field approximation of pressurized fractures*. PhD thesis, Westfälische Wilhelms-Universität Münster, 2019.
- [73] E. Storvik, J. W. Both, J. M. Sargado, J. M. Nordbotten, and F. A. Radu. An accelerated staggered scheme for variational phase-field models of brittle fracture. *Comput. Methods Appl. Mech. Engrg.*, 381:113822, 2021.
- [74] F. Tröltzsch. Regular Lagrange multipliers for control problems with mixed pointwise control-state constraints. *SIAM J. Optim.*, 15(2):616–634, 2004/05.
- [75] J. Wambacq, J. Ulloa, G. Lombaert, and S. François. Interior-point methods for the phase-field approach to brittle and ductile fracture. *Comput. Methods Appl. Mech. Engrg.*, 375:Paper No. 113612, 27, 2021.
- [76] T. Wick. An error-oriented Newton/inexact augmented Lagrangian approach for fully monolithic phase-field fracture propagation. *SIAM J. Sci. Comput.*, 39(4):B589–B617, 2017.
- [77] T. Wick. Modified Newton methods for solving fully monolithic phase-field quasi-static brittle fracture propagation. *Comput. Methods Appl. Mech. Engrg.*, 325:577 – 611, 2017.
- [78] T. Wick. *Multiphysics Phase-Field Fracture: Modeling, Adaptive Discretizations, and Solvers*, volume 28. Walter de Gruyter GmbH & Co KG, 2020.



- [79] B. Winkler. *Traglastuntersuchungen von unbewehrten und bewehrten Betonstrukturen auf der Grundlage eines objektiven Werkstoffgesetzes für Beton*. Innsbruck University Press, 2001.
- [80] J.-Y. Wu, Y. Huang, and V. P. Nguyen. On the BFGS monolithic algorithm for the unified phase field damage theory. *Comput. Methods Appl. Mech. Engrg.*, 360:112704, 23, 2020.
- [81] J.-Y. Wu, V. P. Nguyen, C. Thanh Nguyen, D. Sutula, S. Bordas, and S. Sinaie. Phase field modelling of fracture. *Adv. Appl. Mech.*, 53, 09 2019.